Shape stable composite phase change material with improved thermal conductivity for electrical-to-thermal energy conversion and storage

Anas Islam[a], A. K. Pandey[a*], R. Saidur[a,b], V.V. Tyagi[c]

[a]Research Centre for Nano-Materials and Energy Technology (RCNMET), School of Engineering and Technology, Sunway University, Bandar Sunway, Petaling Jaya 47500, Malaysia

[b]School of Engineering, Lancaster University, Lancaster, LA1 4YW UK

[c]School of Energy Management, Shri Mata Vaishno Devi University, Katra 182320, Jammu & Kashmir, India.

Abstract

Limited thermal conductivity and leakage of phase change material (PCM) are among the most challenging obstacles that impede their effective applications in real-world scenarios. This study focussed on enhancing the thermal conductivity (TC), address leakage issues and incorporate thermoelectric conversion capabilities by using a single multifunctional scaffold. The shape stable PCM (ss-PCM) composite has been prepared using medium temperature range (~46 °C) commercial grade paraffin wax (PW) as organic PCM while expanded graphite (EG) as an encapsulating scaffold. The composite was prepared using vacuum impregnation method, incorporating various weight percentages (wt.%) of EG. In particular, the three wt.% of EG that has been used to encapsulate PCM are 5% (ss-PCM$_1$), 10% (ss-PCM$_2$) and 15% (ss-PCM$_3$). Then the composite was evaluated for its thermal stability, potential chemical interactions, leakage prevention, optical properties, thermal conductivity and thermo-electric conversion capability. Results revealed that the incorporation of 15 wt.% EG in PCM (ss-PCM$_3$) demonstrated no traces of leakage even after heating the composite at 60°C. In addition, a significant increment of 447% in thermal conductivity and 98% in light absorbance has been observed. However, the composite showed a slight decrement of 13.83% in latent heat related to base PCM. Finally, ss-PCM$_3$ was put through to 500 heating-cooling cycles to evaluate its reliability and potential defects due to thermal fatigue. The characterization results of the composite were in close agreement before and after the thermal cycling, indicating its potential for practical applications. The electro-thermal conversion measurement findings indicate that the ss-PCM$_3$ can achieve a conversion ability of 61.89% when operated at 4.8 V. Several potential applications for this composite include energy-efficient buildings, infrared thermal concealment, solar energy utilization, and heat insulation.

* Correspondence: adarshp@sunway.edu.my (A.K. Pandey);

Graphical Abstract.
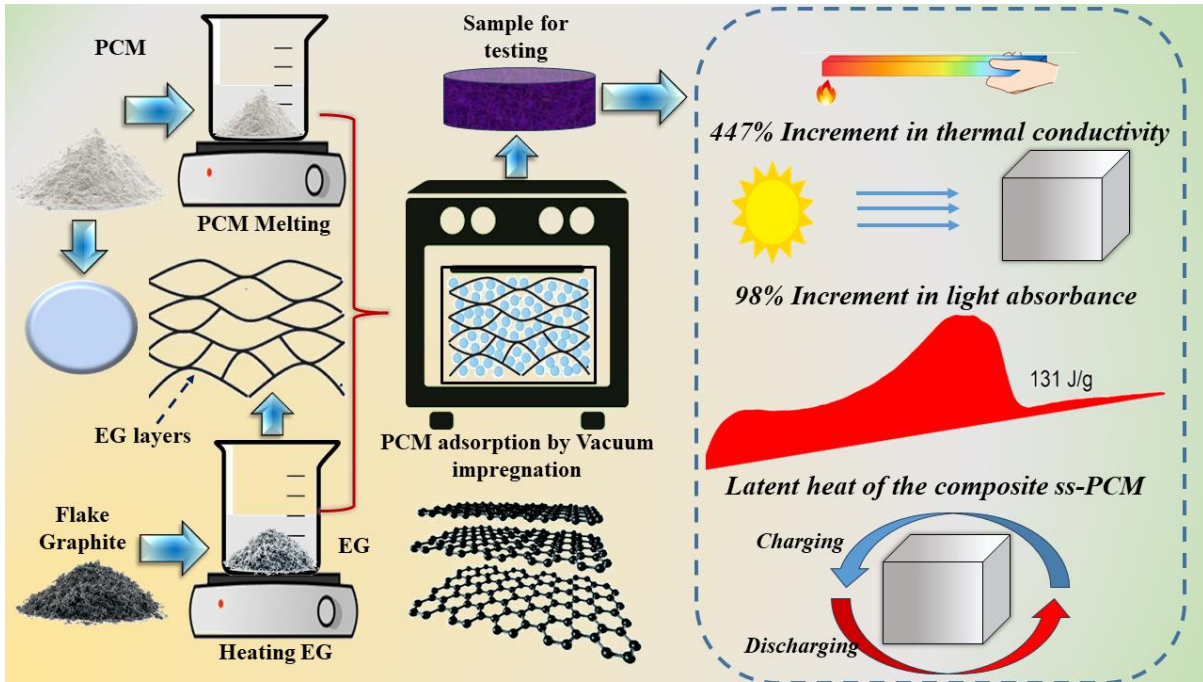
1. Introduction

In past few years, PCM has garnered a substantial attention in heat energy storage (HES) applications due to their high-energy storage densities, operational simplicity, and transformative industrial potential [1], [2]. This facilitates the effective retention of heat energy at consistent temperature that aligns with the phase transition temperature of the utilized application for energy storage [3]. TES find extensive application across various industries, including solar energy, waste heat recovery, battery thermal management, water desalination and electronic devices cooling [4]. There are two foremost types of PCMs viz organic and inorganic. Organic PCMs are generally non-corrosive and found to be chemical stable [5], abundantly available, relatively inexpensive, and easy to work with. However, one disadvantage of organic PCMs is that they have lower TC compared to inorganic PCMs [6]. To enhance TC of base PCM numerous works have been accompanied. For instance, Ji et al.[7] provides evidence that the incorporation of ultrathin-graphite foams (UGFs) into a PCM at volume fractions ranging from 0.8-1.2 vol% may significantly enhance its TC up to 18 times, without causing much alteration to melting temperature and latent heat. In their study, Han et

56 al.[8] used a cross-linked polymer swelling approach to develop a form-stable composite PCM

57 with an improved TC of 1.28 $Wm^{-1} K^{-1}$.

58 Another challenge of using PCMs is their potential for leakage during process of shifting of its

59 phase from solid to liquid [9]. To make the composite leakage proof, researchers have

60 developed shape-stabile PCMs (ss-PCMs), which are composite materials that combine a PCM

61 with a porous supporting matrix [10]. The supporting matrix helps to contain the liquid PCM

62 and block leakage during the phase change process. There have been many studies that have

63 worked on controlling the leakage problem in PCMs. For instance, Marske et al. adopted

64 porogen-aided in situ sol-gel activity for synthesizing monolithic ss-PCMs with superior

65 mechanical immovability [11]. In their 2022 study, Luo et al. [12] tackle the trade-off between

66 constructing shape stable organic PCMs with high enthalpy values and low leakage rates. They

67 present a novel hydrogel composed of reduced graphene oxide (rGO) and covalent organic

68 framework (COF), resulting in an ultralight aerogel with a hierarchical porous structure. This

69 aerogel exhibits exceptional absorption and affinity for organic solvents, enabling the synthesis

70 of shape-stable composite PCMs with outstanding leak resistance, particularly in adsorbing

71 molten organic PCMs like polyethylene glycol (PEG). The COF's superior affinity for PEG

72 results in a remarkable 96.1 wt.% loading rate, surpassing rGO aerogel by 1.7 wt.%.

73 Additionally, the COF reduces PEG/rGO−COF subcooling by 20.3%, demonstrating the

74 composite's high enthalpy (164.6 J/g) and relative enthalpy efficiency (97.4%), highlighting a

75 promising direction for high-enthalpy organic PCM composite preparation. In an additional

76 investigation, Li et al. (2021) [13] introduce a pioneering strategy to augment the crystallization

77 process of PEG phase change materials (PCMs). Their inventive method involves manipulating

78 a matrix with polydopamine and silver nanoparticles, finely tuning pore systems and hydrogen

79 bonding forces. This modification results in the adhesion of PEG PCMs onto mesoporous

80 silica, showcasing remarkable chemical compatibility and a substantial 34.0% increase in

81 thermal conductivity. The resultant shape-stabilized PCMs display exceptional thermal

82 reliability after 10 cycles, underscoring their promising potential for practical applications in

83 alleviating the energy supply-demand contradiction. Trigui et al. enhanced the performance of

84 TES system by incorporating ss-PCMs composite composed of LDPE, hexadecane, and SEBS,

85 with the addition of copper oxide [14]. A different type of ss-PCM was prepared by

86 amalgamation of polystyrene-block-poly(ethylene-ran-butylene)-block-polystyrene triblock

87 copolymer and PCM [15]. In another research study a shape-stable polyethylene glycol (PEG)

88 PCM was prepared within the novolac colloidal structure using sol-gel in situ polymerization

89 process with negligible leakage [16]. Ma et al. [17] engineer a high-performance composite

phase change material by encapsulating PEG in a dual-network hydrogel modified with Ti_3C_2Tx MXenes and silver nanowires (AgNWs). The resulting composite demonstrates superior thermal conductivity (0.64 W/m·K), an 88.9% photo-thermal conversion efficiency, and exceptional energy storage capability with 90.1% PEG loading. In a subsequent work, the researchers claimed to successfully obtain shape-stabilized composite PCMs (ss-PCMs) by impregnating paraffin (PA) into polymethylsilsesquioxane aerogels [18]. A ss-PCM composite (paraffin/HDPE/EG) through melt blending and mould processing method, HDPE helps to restrict the PCM leakage [19]. Luo et al. (2023) develop a high-performance composite phase change material (PEG/PVA-rGO) with outstanding PEG loading (96.9 wt%), elevated photothermal conversion efficiency (88.2%), and enhanced thermal conductivity (0.348 W/m·K) [20].

There have been several works done to make ss-PCM using expanded graphite (EG) as a porous support. For example, a ss-PCM composite mixture was developed employing impregnation and dispersion manner, combining PEG 1000 as PCM and EG [21]. Wang et al. [22] introduced a composite phase change material by embedding hydrated salt into organic paraffin and stabilizing it with expanded graphite (EG). The resulting composite demonstrates excellent shape stability, enhanced thermal conductivity as well as high latent heat (196.6 J/g). A study combined EG with $MgCl_2·6H_2O$–Mg $(NO_3)_2·6H_2O$ eutectic inorganic PCM to develop a composite with high thermal conductivity [23]. Another study prepared a $CaCl_2·6H_2O$/EG composite as a novel form-stable composite PCM through vacuum impregnation method [24]. In their study, Rathore et al. (2021) examined collective outcome of EG and Expanded Vermiculite on thermophysical features of a cost-effective commercial PCM (OM37) and its effectiveness in maintaining temperature within a building component. The study revealed that incorporating 7 wt.% of EG PCM, enhances the TC by 114.4%. Remarkably, the developed ss-PCM maintained its desired properties despite 1000 heating and cooling cycles [25]. Wang et al. (2021) devised a ss-PCM composite by combining Na_2CO_3–K_2CO_3 with EG and coal fly ash (CFA) for high-temperature TES application. The incorporation of EG into these composites led to notable changes in the morphology causing an increase in surface area and pore size. However, addition of EG has slightly decreased its specific heat capacity and latent heat of the ss-PCMs, however, notable enhancement found for thermal conductivity [26].

Nevertheless, ss-PCMs encounter certain limitations, obstacles, and deficiencies that restrict their effectiveness and applicability. ss-PCM often exhibit a relatively low level of thermal conductivity. Several techniques have been used to enhance TC, including the incorporation of fillers, the introduction of pores, and the development of composites [27]. Nevertheless, it is

124 important to acknowledge that these methodologies may also yield adverse consequences,

125 including increasing cost, complexity, and density, or affecting stability and compatibility. One

126 additional obstacle associated with ss-PCM pertains to the need for satisfactory interfacial

127 adhesion and wettability between the supporting matrix and the PCM. This is crucial to achieve

128 consistent distribution and encapsulation. Additionally, the encapsulation procedure of PCMs

129 may need the use of non-eco-friendly substances such as plastics or other materials. Previous

130 research have demonstrated that the mass fraction of PCM absorbed in the supporting

131 framework determines latent heat of final developed composite PCM. [28], [29]. An increase

132 in the mass percentage of PCM inside supporting matrix leads to a corresponding increase in

133 its latent heat storage capacity. While the use of high-thermal conductivity fillers may improve

134 TC of PCM, it is crucial to reduce quantity of fillers to maintain its latent heat [7]. Therefore,

135 in this study an attempt has been made to reduce the filler quantity by using a single

136 multifunctional scaffold to target the major limitations of base PCM viz, thermal conductivity

137 and leakage without a significant drop in the heat storage capacity compared to binary or

138 tertiary composites. Additionally, the developed ss-PCM composite would further be tested for

139 its potential to electric to thermal conversion.

140 In this context, the combination of paraffin wax-A46 (PW-A46) PCM with expanded graphite

141 (EG) as a conductive filler in ss-PCMs represents a novel and unexplored avenue. This

142 commercial grade A46 paraffin was selected as PCM owing to its some advantageous

143 properties such as medium phase transition temperature (˜45-50 °C) for energy-efficient

144 building temperature regulation, prevent overheating in sensitive components, electromagnetic

145 interference (EMI) shielding, non-toxicity, high LHTES capacity (over 150 J/g), non-

146 corrosiveness, nonflammability, good chemical stability, low volumetric changes during phase

147 transition, and large-scale availability [30]–[32]. For example, Gong et al. [33] created a

148 versatile flexible phase change composite film using a one-step vacuum-assisted filtration

149 method, showcasing high efficiency in light-to-thermal conversion, Joule heating generation,

150 fire safety, and EMI shielding effects.

151 Although, activated carbon-based additives like CNT, CNF, and graphene could offer superior

152 thermal conductivity and adsorption capacity. However, agglomeration and high costs hinder

153 practical applications [34]. In this regard, expanded graphite (EG) emerges as a valuable

154 alternative with better dispersion, significant PCM adsorption capability, and comparatively

155 lower costs than other materials mentioned[25]. The incorporation of EG not only contributes

156 to shape stability and thermal conductivity but also imparts intrinsic fire resistance, showcasing

157 significant potential for safe and effective Li-ion battery thermal management [22]. Table 1

exhibits previous works regarding ss-PCM composites in the similar temperature range highlighting the enhancement in TCs.

Table 1: Comparison of TCs of different organic ss-PCM composites

PCM	Supporting material	PCM Loading (%)	Melting temperature (°C)	Thermal conductivity	Reference
Nonadecane	Activated carbon + EG	75	30.14	0.83	[34]
Polyethylene glycol (PEG)	Lignin-based ordered porous carbon (LOC)	70	---	0.5029	[35]
		75		0.5847	
Paraffin (PA)	Iron tailing	68.82	50.82	0.73	[36]
	Magnetite	50	57.93	0.53	[37]
	Perlite	53.40	50.40	0.40	[38]
hexadecanol	porous aerogel	69.4	49.15	0.421	[39]
Paraffin	EG	85	~46	1.01	This work

The highlighted advancements and comparisons with previous works serve to underscore the significance and innovation of the developed materials. By showcasing a 447% increase in thermal conductivity, improved shape stability, and substantial gains in both thermal and light absorption capabilities, the PW-A46 with expanded graphite surpasses or significantly improves upon prior achievements in similar studies. The electro-thermal conversion measurement results further emphasize the material's exceptional performance, providing a clear benchmark for the novel advancements and positioning the work as a notable contribution to the field. By employing EG to disperse and stabilize the PCM within the matrix, the resulting composite can achieve both enhanced shape stability as well as enhanced TC. This unique composite was analysed using SEM and FTIR to investigate its microstructure, morphology, and compatibility. THB (transient hot bridge), TGA (thermogravimetric analysis) and DSC (differential scanning calorimetry), were used to calculate TC, heat storage capacity, and decomposition temperature. The thermal reliability of composite for 500 cycles were also analysed to ensure their stability and suitability. This comprehensive analysis provides valuable insights into the composites' microstructural, thermal, mechanical, and reliability aspects, contributing to a better understanding of their potential application in medium temperature range. The significance of this study lies in its potential to contribute to the advancement of ss-PCM for energy storage application. This work has important implications for improving

180   energy efficiency and reducing greenhouse gas emissions. This would be helpful in achieving

181   the United Nations' Sustainable Development Goals (SDGs), particularly Goal 7 and 13.

182

183   ## 2. Materials and Experimental Procedure

184   *2.1. Materials*

185   In this study, organic PW-A46 PCM with melting point of 46 °C and TC of 0.21 W/m·K

186   obtained from PCM Products Ltd. Additionally, flake graphite (FG) powder purchased from

187   ACS Material, LLC, located in Pasadena, CA, was utilized, with an expansion rate ranging

188   from 220 ml/g to 300 ml/g. A comprehensive overview of the thermophysical properties of

189   PW-A46 and EG are tabulated in Table 2.

190   *Table 2: Thermophysical properties of PW-A46 and additives*

Materials	PW-A46	Expanded Graphite
Phase Transition Temperature (°C)	˜46 °C	3,652- 3,697 °C
Density (kg/m^3)	910	300
Heating Enthalpy (J/g)	153	---
Thermal Conductivity (W/m·K)	0.21	50 -100
Particle Size	---	< 50 μm
Colour	White	Silvery – grey to black
Purity	---	> 97%

191

192   *2.2. Expanded Graphite Preparation*

193   The porous EG scaffold was created by exfoliating flake graphite (FG) with potassium

194   persulfate ($K_2S_2O_8$) under concentrated H_2SO_4 at a temperature of 80 °C. Initially, 1 gram of

195   FG was mixed with a predetermined amount of concentrated H_2SO_4. Afterward, while stirring

196   continuously at room temperature, $K_2S_2O_8$ was incorporated into it. Once the mixture was

197   thoroughly homogeneous, it was moved to water bath at 80 °C for 5 minutes to produce

198   acidified EG. Ultimately, the obtained acidified EG was subjected to a neutralization procedure

199   using distilled water under vacuum filtration following by drying in an oven at 60 °C for 5

200   hours, yielding the final form of EG [40]. Fig. 1 (a) presents SEM images of FG while Fig. 1(b)

201   depicts the SEM image of EG. FG exhibited a sheet-like structure with tightly packed layers

and a smooth surface. In contrast, EG displayed a distinct morphology, characterized by a worm-like fluffy shape [41]. This transformation occurred due to the decomposition of potassium persulfate, which resulted in the release of gases within the graphite layers [40], [42]. Graphite rapidly expanded along its C-axis direction as increasing pressure from gases overcome van der Waals forces between interlayers. These observations highlight significant differences in morphology between FG and EG.
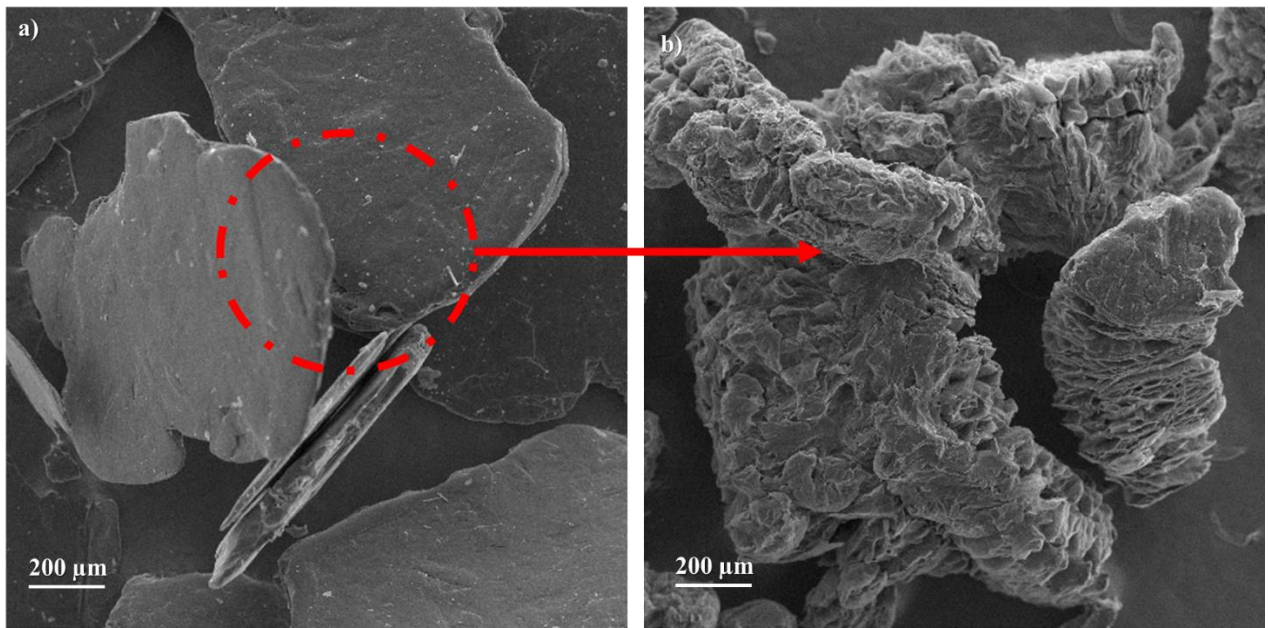
Fig. 1 SEM images of (a) Flake Graphite (b) Expanded Graphite

2.3.Preparation of ss-PCM composite

In this study, three samples of PCM composite with varying wt.% of EG namely, (PW-A46/5%EG) ss-PCM$_1$, (PW-A46/10%EG) ss-PCM$_2$ and (PW-A46/15%EG) ss-PCM$_3$ were prepared. Initially, a specific quantity of PCM was kept in beaker and subjected to heating at 60°C until it melted completely [43]. Besides, melted PCM was added with the treated EG samples, capillary force and surface tension enabled PCM to be completely adsorbed into EG. The mixtures were kept at 60°C for 24 hours and exposed to intermittent mixing by magnetic stirring for 5 minutes every 8 hours to ensure specific adsorption. Then the resulting powdery PCM composite was pulverized into tablets to evaluate the thermophysical properties. The ss-PCMs were developed using the vacuum assisted melt impregnation (vacuum impregnation) with magnetic stirring method, as shown in Fig. 2.
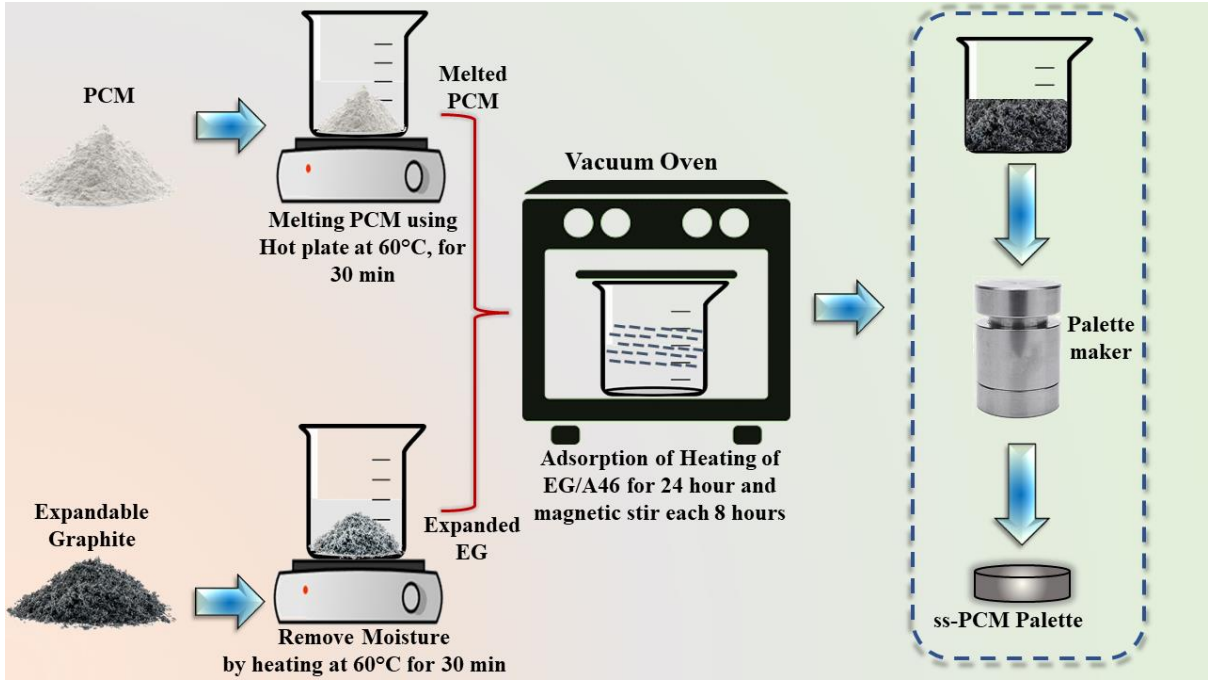
Fig. 2. Representation of ss-PCM composites preparation

2.4. Characterizations and thermal cycle testing instruments

In this study, the morphology of ss-PCM was investigated using a TESCAN VEGA 3 scanning electron microscope (SEM) with VEGAS software. The chemical characteristics were analysed via Fourier-transform infrared spectroscopy (FT-IR) instrument obtained from PERKIN ELMER, USA. It covers a wavenumber range of 400-4000 cm^{-1} with a spectral accuracy of 0.01 cm^{-1}. The light transmissivity and absorbance was evaluated through LAMBDA 750 UV-Vis spectroscopy obtained from Perkin Elmer, USA. The wavelength range of 280-1400 nm to encompass the UV, visible and infrared regions has been taken for measurements. The thermal conductivity of the ss-PCM was determined using the Transient Hot Bridge (THB-500) technique with Linseis Hot Point Sensors (HPS) across a wide temperature range from -150 °C to 700 °C. The transient plane source approach provided precise and accurate results with a precision of over 1% and an accuracy of over 5%. Melting point and latent Heat-storage capabilities were assessed with DSC 3500 (Sirius, NETZSCH) analysis with a heating rate of 5 °C min^{-1} under N_2 environment between 20 °C and 80 °C. Further, heat storage capacity have been estimated using Equation (1),

$$\Delta H_{ss-CPCM} = \eta \times \Delta H_{PCM} \dots \dots \dots \dots (1) \ [25]$$

where H_{ss-PCM} is theoretical latent heat, η is percentage of PCM in composite overall mass, and H_{PCM} is PCM's experimental latent heat. To examine thermal reliability of ss-PCM, 500 heating-cooling cycles were conducted using a customized copper plate model with controlled

9

temperature ranging from 30 to 70 °C at 15 °C min^{-1} given steady environmental circumstances. Furthermore, a leakage test evaluated the ss-PCM leakage-proof performance by subjecting specimens to 60 °C (~15 °C above PCM melting point) for 45 minutes inside an oven over filter paper. Additionally, to determine the rate of leakage in shape stabilized (ss-PCMs), the weight of each sample was recorded at 10-minute intervals, with a total of three measurements taken. The initial weight of the sample was denoted as M_o, whilst the weight of the sample that remained after being subjected to heating for a duration of n hours was represented as M_n. After applying heating, the leakage rate (L_{rn}) for each specimen was determined by using the equation (2) [44]:

$$L_{rn}(wt.\%) = \frac{M_o - M_n}{M_o} \times 100 \dots\dots\dots\dots\dots (2)$$

The efficiency (φ) for electrical-to-thermal energy transition of developed ss-PCM was determined using Equation (3) [45].

$$\varphi = \frac{m\Delta H}{UI_e t} \dots\dots\dots (3).$$

The variables m and ΔH represent the mass and latent heat of the composite ss-PCM respectively [45]. I_e represents electric current flowing through the circuit, U denotes the voltage applied, and t signifies elapsed time.

The enthalpy efficiencies for our obtained DSC values of latent heat for all the composites can be calculated by equation (4) as:

$$\lambda = \frac{\Delta H_{H(ss-PCM)}}{\Delta H_{H(PCM)}}\dots\dots.(4)[46]$$

where $\Delta H_{H(ss-PCM)}$ and $\Delta H_{H(PCM)}$ mean the melting enthalpy of ss-PCMs and pure PCM, respectively.

2.5. Uncertainty analysis of measuring instruments

The study of uncertainty in measuring devices is a significant and complex undertaking that requires a comprehensive understanding of measurement procedure, origins and impacts of uncertainty, and the techniques and resources for evaluating and expressing uncertainty [47]. The utilization of uncertainty analysis may enhance the calibre and dependability of measures, as well as facilitate the effective communication of outcomes and their constraints to users and clients. Table 3 includes the different equipment used in this study along with deviation errors.

Table 3: Summarizing the uncertainty analysis of the equipment used in the study:

Equipment	Measurement type	Max. Deviation	Instrument error	Scale

10

Weight balance	Weight of PCM and fillers	---	0.001 g	0.0001 g
TGA	Mass loss	±5 mg	±0.24 %	20-600 °C
	Temperature	±0.4 °C	NA	
THB	Thermal conductivity	NA	±10 %	0.02-2.0 (W/m·K)
DSC	Latent heat	±1.15 J/g	±0.2 %	50-600°C at 0.001 to 1000°C per min
	Melting point	±0.11 °C		
Uv-Vis	Absorption / Transmission	---	±0.1 %	200 nm-3300 nm

274

This study examines the methodology proposed by McClintock and Kline for evaluating the level of uncertainty associated with measurement devices [48]. The evaluation of experimental uncertainty is accomplished using mathematical equations 4 as:

$$U_Q = \sqrt{\left[\left(\frac{\partial r}{\partial y_1}\right)^2 (z_1)^2 + \left(\frac{\partial r}{\partial y_2}\right)^2 (z_2)^2 \dots\dots\dots\dots + \left(\frac{\partial r}{\partial y_n}\right)^2 (z_n)^2\right]} \dots (5)$$

Where, w_r represent the uncertainty associated with the outcomes. R is a predetermined function of the independent variables (Y_1, Y_2, ..., Y_n), and (Z_1, Z_2, ..., Z_n) represents the uncertainties associated with the independent variables. The assessment of uncertainty in measuring thermophysical properties for this investigation was conducted prior to expanding the experiment via the use of several methodologies. The amount of uncertainty detected in this study was found to be less than 5%, indicating a high level of accuracy in the instruments used for the present research.

3. Results and Discussion

3.1. Analysis of chemical interactions and functional groups

The Fourier transform infrared (FTIR) spectroscopy was utilized to assess chemical interaction between PCM and EG. Paraffin wax is a hydrocarbon compound classified as an alkane, characterized by its chemical formula C_nH_{2n+2}. It is composed of linear hydrocarbon molecules, with the value of n ranging from 20 to 40. The non-linear nature of paraffin molecules can be attributed to the sp3 hybridization of each carbon atom. Consequently, paraffin with a chemical structure of C_nH_{2n+2} is expected to display a total of (3n-6) vibration modes [30]. Out of the total number of vibrational modes of paraffin molecules, which is represented by the equation 3n-6, only four modes are found to be infrared (IR) active. These specific modes are discovered

and associated with peaks observed at a particular wavenumber. The observed wavenumbers are 2847, 2916, 1471, 1366 and 715 cm^{-1} [49]. The FTIR spectral curve of the prepared ss-PCM is shown in Fig. 3. The wavenumber 2916 cm^{-1} conforms to symmetrical vibrational stretching of $-CH_3$, where bond length rises equally. Similarly, the wavenumber 2847 cm^{-1} corresponds to the symmetrically vibration of stretching of $-CH_2$. The presence of a peak at a wavelength of 1471 cm^{-1} indicates the occurrence of deformation vibration, specifically the change in bond angles, in both the $-CH_3$ and $-CH_2$ groups [50]. The last peak observed at a wavelength of 715 cm^{-1} indicates to rocking vibration, which involves angular bending of bonds in both clockwise and anticlockwise directions within the same plane, namely within the $-CH_2$ group [51]. All PCM composites, exhibit spectral curves like those base PCM, indicating that the EG and PCM are physically intermingled. Lacking carboxyl groups, the EG does not exhibit IR activity or generate peaks when exposed to IR radiation. In addition, the absence of any additional peaks or chemical reactions confirms that ss-PCM exhibit excellent compatibility with EG and no of chemical interactions.
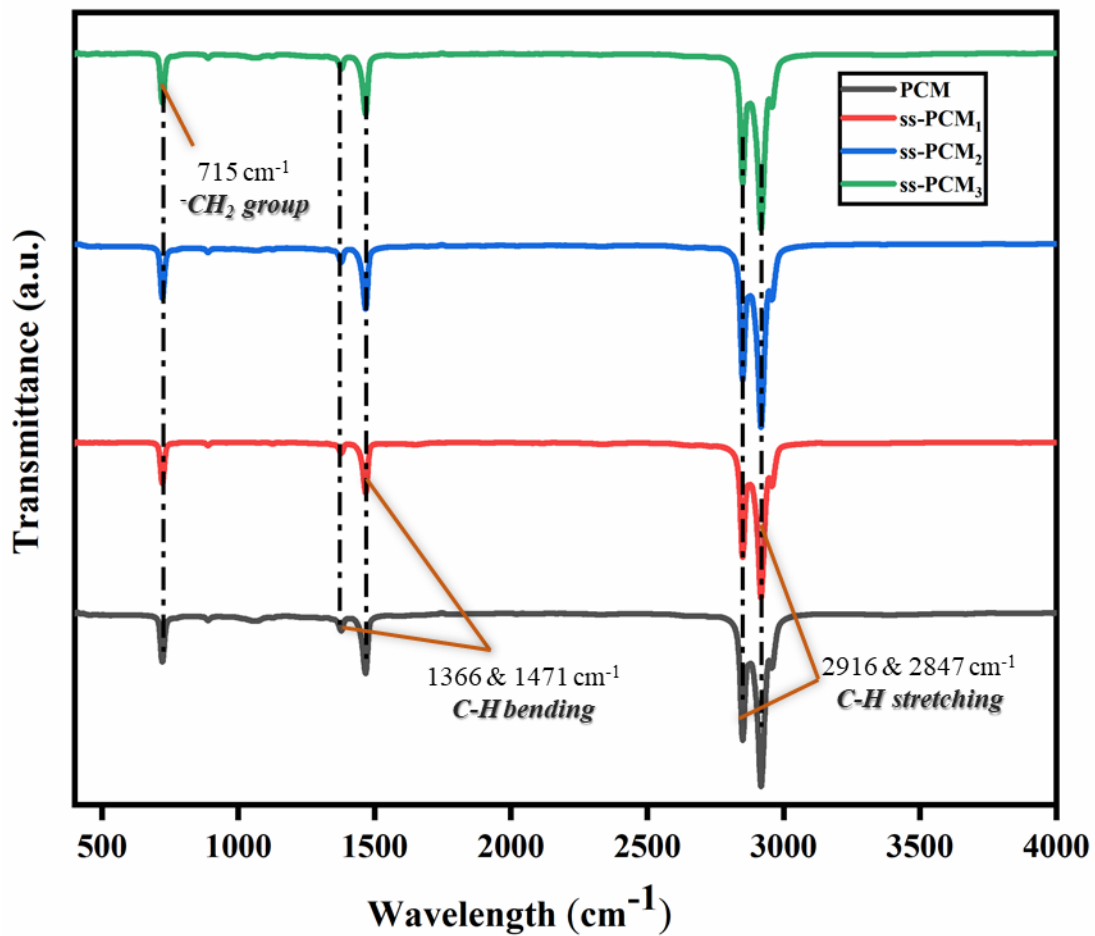
*Fig.3. Functional group peaks*

12

3.2.Morphology and microstructure of PCM, EG and ss-PCM composite

314   The scanning electron microscope (SEM) can be utilised to examine the morphological

315   characteristics of the PCM, EG, and the resulting ss-PCM. Fig. 4 (a) illustrates the SEM image

316   of base PCM, it showcases its intricate microstructure at a high-resolution level. The SEM

317   images depict a well-defined and homogeneous morphology with a smooth and even surface.

318   The microstructures of PCM exhibit a consistent distribution of its constituent elements,

319   revealing its compositional uniformity. Further, these SEM images shows the presence of

320   unique crystalline domains of PCM, indicating its organized lattice structure at the microscale.

321   The absence of significant defects or irregularities on the surface suggests a high level of

322   material purity and structural integrity. The application of thermal treatment induces the

323   partitioning of a significant proportion of the carbon layers within the FG material, leading to

324   the formation of a cellular morphology characterised by the presence of multiple carbon layers

325   composing the walls of each individual cell. Further, because of the porosity related with local

326   separation, the total volume of EG increases while the density decreases in comparison to FG.

327   The surface of the EG displays an interweaving arrangement of numerous worn like structures

328   [52]. As shown in Fig. 4 (b) these honeycomb structures enable the EG to exhibit excellent

329   adsorption properties [53]. Additionally, when the PCM undergoes melting, the presence of

330   these honeycomb capillaries effectively prevents any potential leakage. The SEM images in

331   Fig. 4 (c-e) depict the composite ss-PCM$_1$, ss-PCM$_2$ and ss-PCM$_3$ at different weight

332   percentage of EG. Upon observing Fig. 4 (c), it becomes evident that even after the PCM has

333   been adsorbed into pores of EG, worm-like structure of expanded graphite remains intact. Upon

334   increasing content of expanded graphite (EG) in ss-PCM composite, surface features of sample

335   underwent noticeable changes. The PCM phase initially had smooth features, but these

336   disappeared, leaving only the lamellar structure of the expanded graphite. This suggests that at

337   an EG content of 10%, the PCM was absorbed into the composite's pore structure, as shown in

338   Fig. 4 (d). However, the presence of noticeable clusters of block and strip paraffin on the

339   surface suggests an excess of paraffin relative to the absorption capacity of the EG.

340   Furthermore, the capillary force of the EG appears to be insufficient, leading to the

341   accumulation of paraffin on both the pore surface and within the pores. With further increases

342   in EG content viz., 15%, as evident from Fig. 4 (e) the surface pore structure of the ss-PCM$_3$

343   composite became more distinct, indicating a stronger effect of PW-A46 adsorption. All the

344   PCM has been absorbed by the EG in ss-PCM$_3$ composite. The uniform distribution of the

345   absorbed paraffin inside the ss-PCM$_3$ composite, because of capillary pressure and force of

346   surface tension of porous EG [54]. EG forms a stable layer that reduces interfacial tension,

347 promotes better wetting, and prevents aggregation or migration of paraffin droplets, resulting

348 in a homogeneous distribution of paraffin throughout the composite material. Additionally, for

349 better understanding and visualization, more SEM images at different magnifications have

350 been included in the supplementary document as Fig. S1. These supplementary images offer a

351 more comprehensive view.
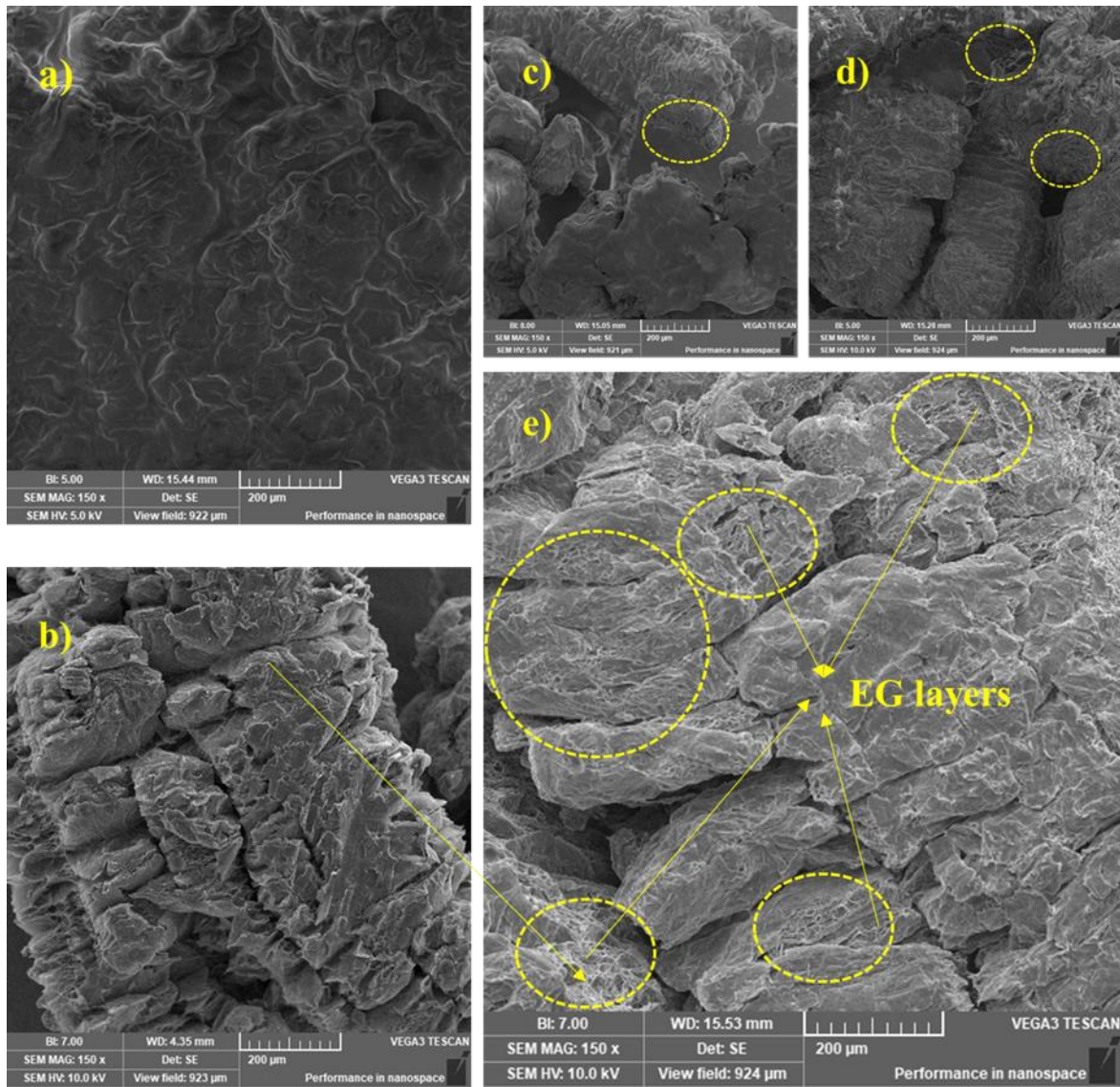
353 *Fig. 4. Morphological SEM image of (a)base PCM, (b) expanded graphite (EG), (c) ss-*
354 *PCM₁, (d) ss-PCM₂, (e) ss-PCM₃*

355 The inclusion of micro-meso pores within the system plays a pivotal role in establishing a

356 heightened capillary effect, facilitating the absorption and confinement of the base PCM known

357 (PW-A46). Notably, the capillary and surface tension forces arising from the pores of expanded

358 graphite (EG) act as stabilizing agents for the PCM [55]. This phenomenon results in the PCM

359 being effectively secured within the system through interactions with the capillary and surface

360 forces exerted by the porous structure of EG [56]. Furthermore, the compatibility of EG with

14

organic compounds is crucial in this context, as it enables a seamless attachment of the PW to the surfaces of the graphite layers. This interplay of forces and material compatibility substantiates the successful shape stabilization of the PCM, illustrating the intricate and scientifically significant processes at play in the development of our innovative composite material.

Furthermore, to ascertain the chemical composition of the PCMs, porous additives, and composite PCMs, they were subjected to visualization using energy-dispersive X-ray spectroscopy (EDX). The resulting spectra are presented in supplementary document as Fig. S2. The organic PW-A46 consists primarily of carbon atoms. Fig. S2 (a) demonstrates that the carbon elements within the complex can be observed and recreated through the utilization of EDX spectroscopy. EG is again composed of carbon atoms, and the spectral analysis of EG reveals the existence of carbon, as illustrated in Fig. S2 (b). Similarly, it may be argued that ss-PCMs are mostly a carbon derivative, as evidenced by the presence of a peak corresponding to the element C, as seen in Fig. S2 (c-e). Furthermore, these composite ss-PCMs demonstrates the uniform adsorption of EG enhanced PCMs within the pores of EG material. This observation serves as confirmation of the presence of the created composite sample.

3.3. Optical properties of ss-PCM composite

Most organic PCM exhibit transparency within the electromagnetic spectrum of wavelength range from 280 to 720 nm. Consequently, it becomes imperative to augment the absorption capabilities of these organic molecules within the aforementioned wavelength area in order to optimize their effectiveness in harnessing solar energy. The absorbance of photons by PCM is a critical factor to consider when investigating operational conversion of light energy into thermal energy in TES systems, as solar radiation is the primary input energy source. The light absorbance patterns of the prepared ss-PCMs were investigated through a UV-Vis spectroscopy. The primary sources of solar radiation are concentrated in the ultraviolet (UV) range (7%), visible light range (44%), and near infrared (IR) range (37%). Therefore, light absorance of ss-PCM is examined inside the limits of 280-1400 nm wavelength, which encompasses the UV spectrum (280–380 nm), visible spectrum (380–720 nm), and IR spectrum (720–1400 nm) [57]. Single colour of light is shown through PCM sample. The transmittance and absorbance characteristics of ss-PCM composite sample are shown in Fig. 5 (a) and (b), respectively. Light absorbance, denoted by absorbance (A), serves as a metric for light a material absorbs, as per the Beer-Lambert Law:

$$A = \alpha IC \ldots \ldots \ldots (5)$$

15

Absorptivity (α) is a material-specific parameter defining its intrinsic capacity to absorb light, and it directly influences absorbance. This relationship is contingent on factors like substance concentration (C), light path length (I), and material characteristics, collectively influencing the overall optical behavior of the material. Absorbance is not directly proportional to wavelength, for each substance absorbs light at different wavelengths. Absorbance depends more on the concentration of the solution and its molar absorptivity. Since α is a constant determined by each substance, A (absorbance) is directly proportional to C (concentration). Typically, organic phase change materials (PCMs) exhibit a white colour and show lower absorbance compared to darker materials. However, since the chosen PCM belongs to the alkane family, achieving absorbance requires higher energy due to the necessity for electron σ-σ* orbital transition.
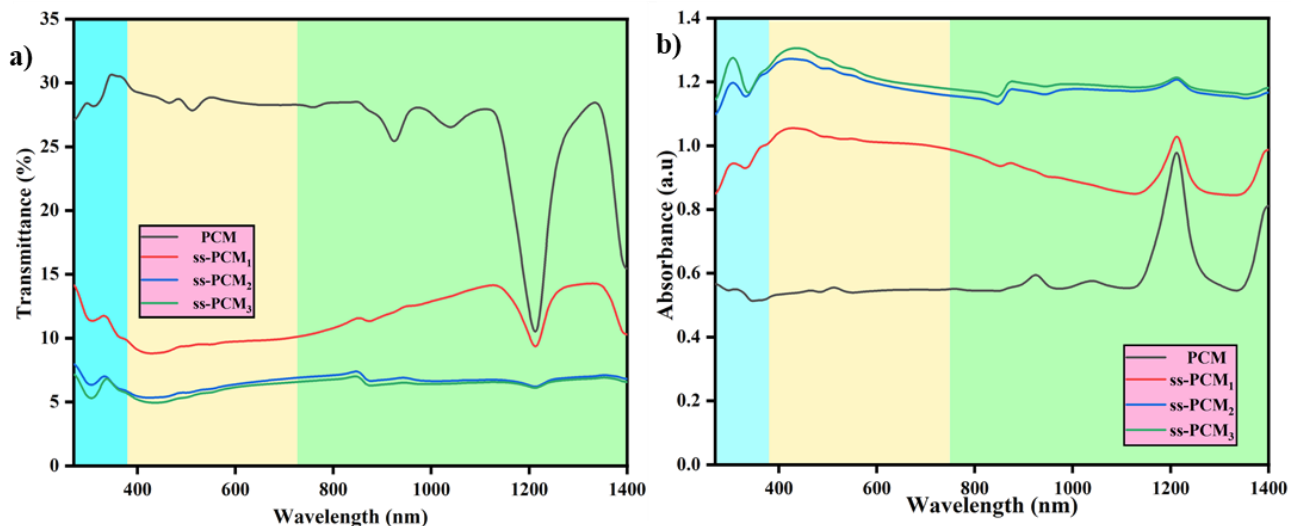
Fig. 5. Solar spectral (a) transmissivity curve (b) absorbance curve of ss-PCMs

Fig. 5 (a) shows, that the transmittance of the composite PCM diminishes as the absorbance rises. Notably, the presence of EG due to its black colour reduces light transmission while increasing absorption. As can be shown in Fig. 5 (b), absorbance of base PCM is around 0.60; however, increasing quantities of EG in composite PCM results in enhanced absorbance of 1.19 due to high energy intensity at shorter wavelengths of UV spectrum. This upward trend in absorbance suggests that adding EG improves the PCM's capacity to absorb solar energy. The transmissibility of the base PCM is resolute to be 27.4%. The transmissibility values for composite PCM samples, ss-PCM$_1$, ss-PCM$_2$ and ss-PCM$_3$ are 10.7%, 6.4% and 6.1%, respectively. These results indicate a reduction in transmissibility as the concentration of EG increases within the PCM. It is essential to consider the inverse link between transmissibility and absorbance. The decreased transmission observed with the addition of EG to the PW-A46

420 PCM is accompanied by increase in absorbance. Enhance in absorbance enables PCM
421 composite to capture and respond to incident solar radiation, facilitating higher thermal energy
422 storage rates more effectively [58]. The increased absorption found in the composite distributed
423 with EG, as opposed to pure PCM, can be attributed to the interaction of many significant
424 variables. When exposed to continuous radiation, transparent organic molecules naturally
425 absorb some of the energy they receive, and this absorption is increased by the dispersion
426 of EG. Photon absorption in the PCM, induced by energy packets from the solar spectrum,
427 causes electrons to shift from lower energy ground states to higher energy excited states. More
428 precisely, in the case of alkanes, this process entails the movement of electrons between σ and
429 σ* orbitals. The increased energy needed for electron transitions in organic molecules is
430 fulfilled by solar radiation [30]. However, the addition of evenly dispersed EG enhances the
431 effectiveness of absorption. The basis for this improvement lies in the many rotational and
432 vibrational movements displayed by molecules under normal circumstances, resulting in the
433 absorption of a broad range of wavelengths. The subtle variations in energy levels related to
434 different forms of stimulation, particularly electronic stimulation, clarify the observed rise in
435 absorbance in the EG-dispersed composite.

436

437   *3.4. Thermal decomposition analysis*
438 To assess thermal stability of organic PCM PW-A46 and its composite with EG, a thermal
439 degradation analysis was conducted using TGA. The study observed the weight percentage loss
440 of the base PCM and composite samples ss-PCM$_1$, ss-PCM$_2$, and ss-PCM$_3$ as the temperature
441 increased. The weight degradation profiles of the samples are presented in Fig. 6. Results
442 indicate that no decomposition occurred up to 200°C. Highest weight loss, about 90%, was
443 observed between 230°C and 300°C as PCM underwent evaporation and degradation. Initiation
444 points of decomposition for composite specimen closely resembled that of base PCM.
445 However, composite samples showed a culmination point of decomposition between 310°C
446 and 330°C, indicating presence of residual EG. All composite samples displayed higher
447 degradation temperatures than base PCM, except for ss-PCM$_3$, which showed slight decrease
448 in degradation temperature due to the formation of micro composites caused by some EG
449 clustering. The TGA curves confirm that EG was effectively dispersed within the PCM, leading
450 to an improvement in the thermal stability of the samples. These findings align with previous
451 research that supports the enhanced thermal stability achieved through other porous-matrix-
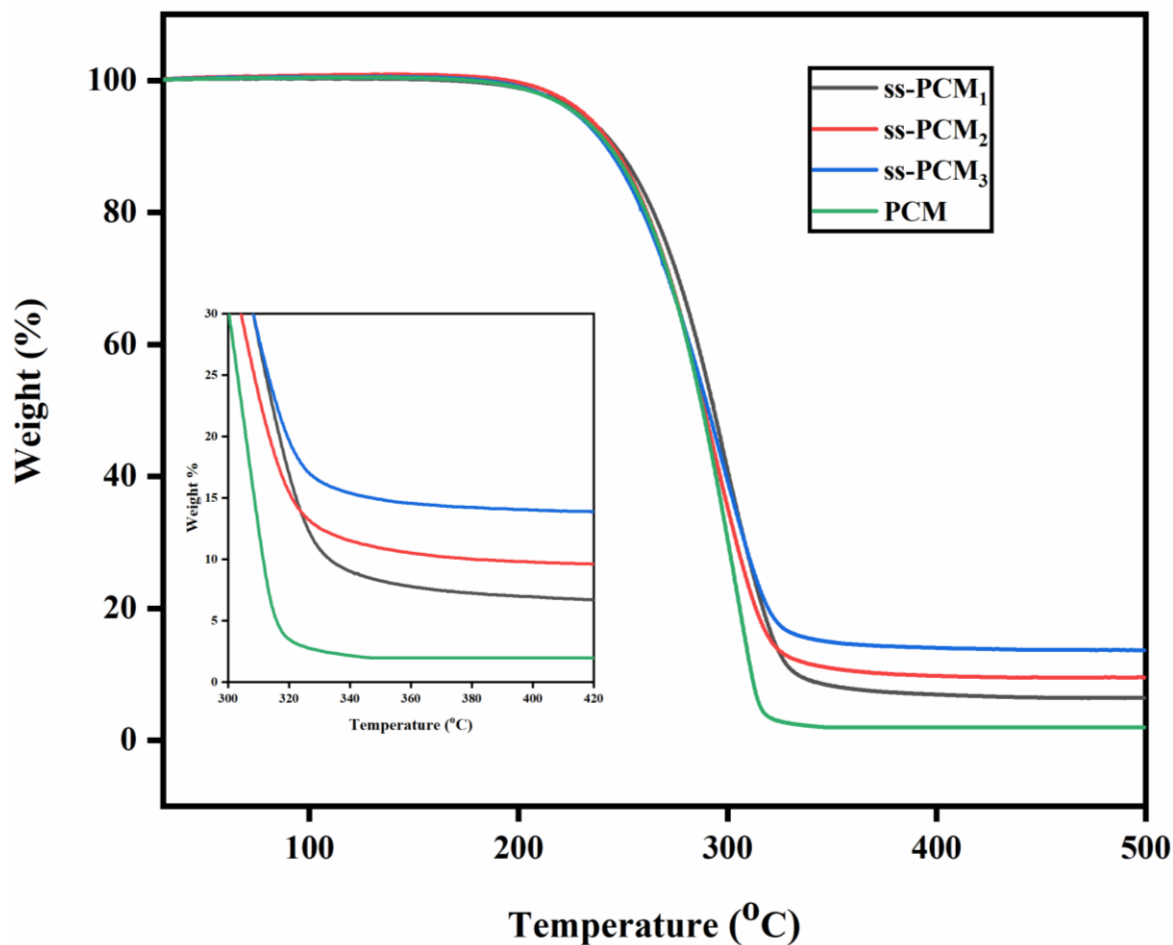452 based shape-stable composite PCMs [44], [59].

Fig. 6. PCM composite thermal degradation analysis at different weight% EG

3.5. Latent heat enthalpy

Latent heat enthalpy is the amount of heat absorbed or released by a material during a phase change, such as melting or crystallization. DSC is used to examine latent heat enthalpy of a material by measuring area under the curve corresponding to phase change of sample in the DSC curve. The latent heat enthalpy can be used to find out heat capacity, the degree of crystallinity, the purity, and the thermal stability of a material. Results of DSC testing for PCM and its composites are presented in Fig. 7. All ss-PCM samples exhibited distinct endothermic and exothermic peaks, which indicated consistent phase change behaviour. Notably, addition of EG to ss-PCM decreased phase change temperatures due to weakened attractive interactions between inner surface of porous media and PCM [60]. The latent heat of melting of PCM and ss-PCM decreases with increasing EG content, due to the dilution effect of the non-melting EG filler and the possible reduction of crystallinity of the PCM matrix. Moreover, introduction of EG enhanced thermal conductivity of composite, which affected PCMs crystallization process [61]. This increased thermal conductivity facilitates faster heat transfer and dissipation,

18

potentially altering PCM's phase change properties. The measured latent heat storage capacity values for ss-PCM samples matched calculated values, as shown in Table 4. The calculated latent heat of melting of ss-PCM is lower than the measured latent heat of melting of PCM, due to the presence of the supporting matrix that reduces the effective PCM content in the ss-PCM.

Table 4 PCM and ss-PCM DSC analysis.

PCM composite sample	Onset melting temperature (°C)	Peak melting temperature (°C)	Measured latent heat of melting H_m (J/g)	Calculated latent heat of melting H_c (J/g)	Enthalpy efficiency λ
ss-PCM (pure PCM)	41.9	47.1	154	154	100
ss-PCM$_1$ (5%EG)	42.2	47.3	145.7	146.3	94.6
ss-PCM$_2$ (10%EG)	42.2	47.4	138.1	138.6	89.6
ss-PCM$_3$ (15%EG)	42.3	47.4	132.7	130.9	85

The DSC findings underscore the significance of taking into account both the phase change temperature as well as latent heat while preparation of ss-PCMs, particularly when including supplementary elements that may have an impact on both characteristics.
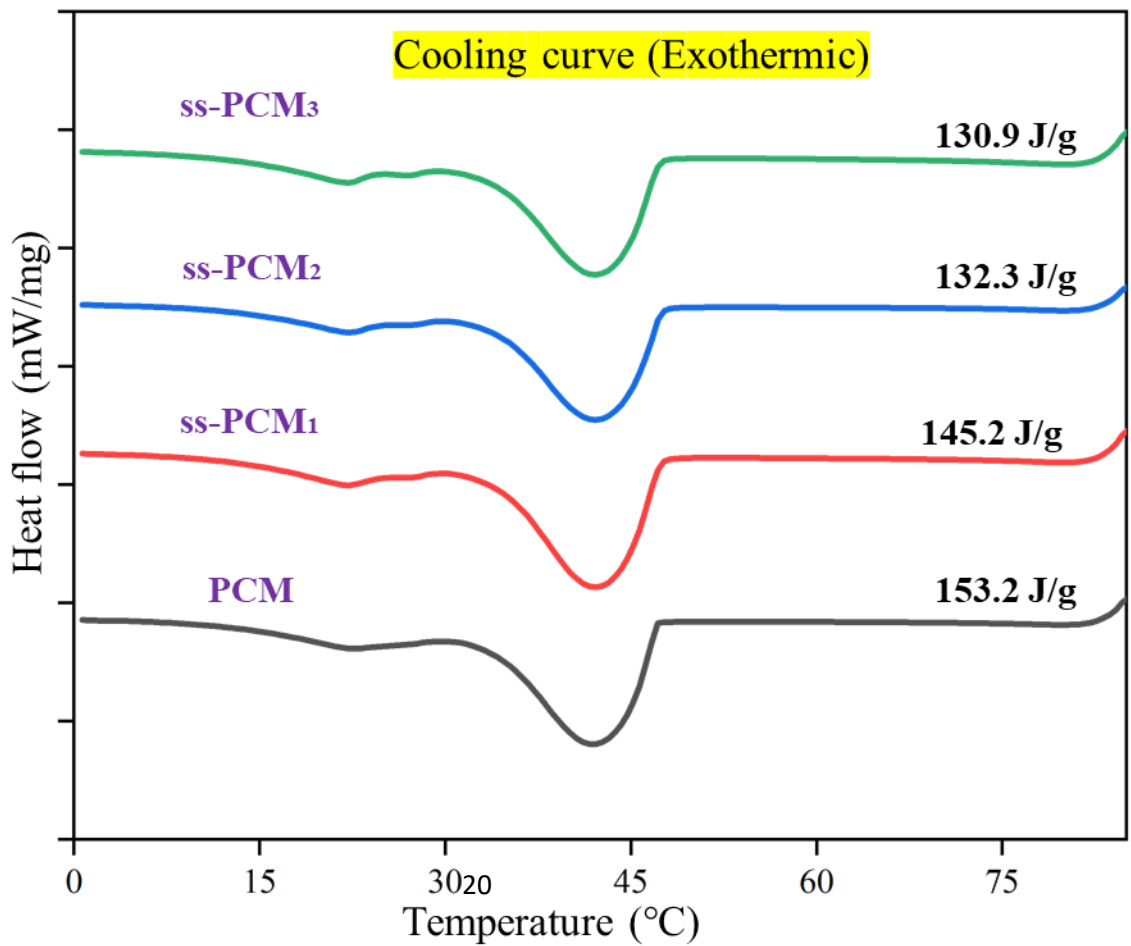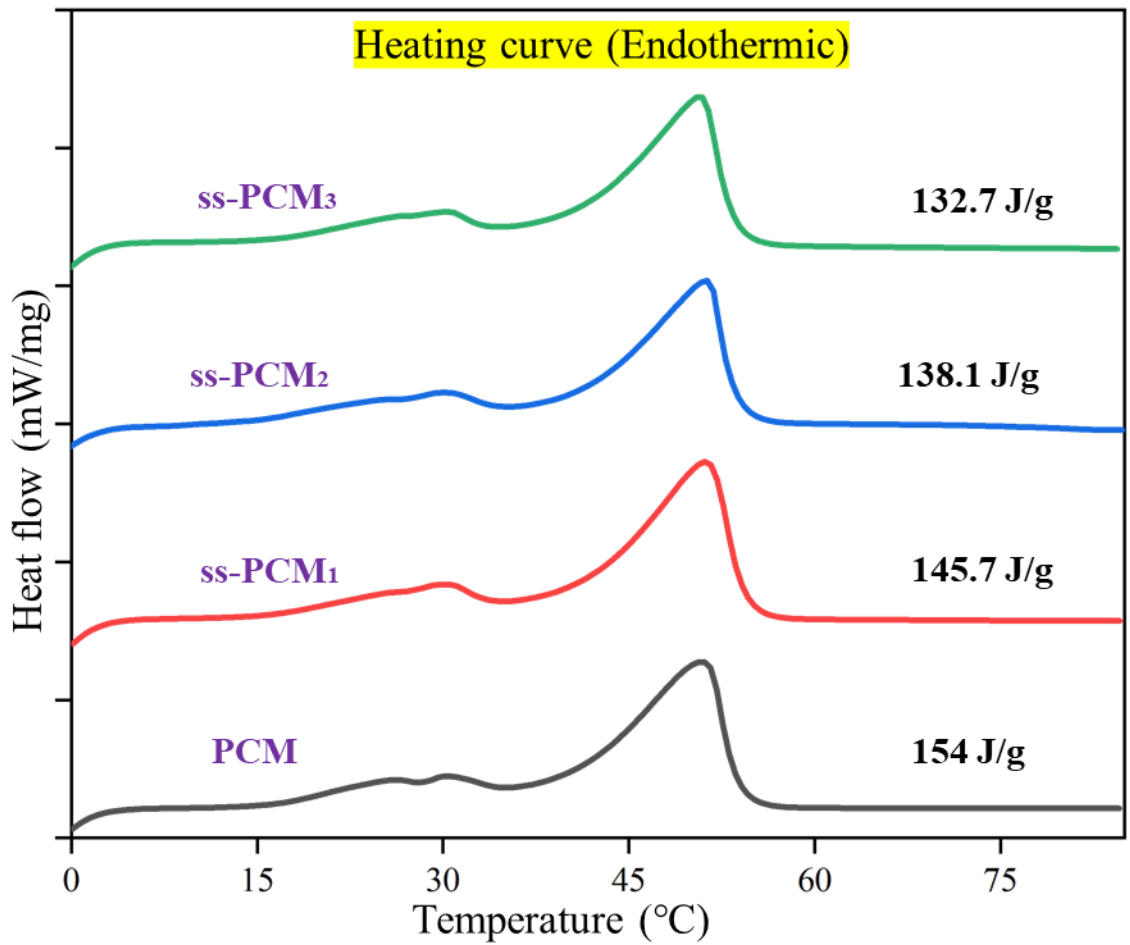
*Fig. 7. Heating and cooling enthalpy curve of ss-PCM composites*

Table 4 presents the results of the DSC analysis for composite samples, including the base PCM and different formulations of ss-PCM with varying percentages EG. The onset melting temperature represents the temperature at which the phase transition begins, while the peak melting temperature indicates the temperature at which the melting process reaches its maximum intensity. The measured latent heat of melting (H_m) represents the amount of heat absorbed or released during the phase transition, measured in joules per gram (J/g). The calculated latent heat of melting (H_c) is an additional parameter obtained by equation (1) [25] that provides an alternative mathematical perspective on the energy absorbed or released during melting.

For the ss-PCM samples with varying percentages of EG (ss-PCM$_1$, ss-PCM$_2$, and ss-PCM$_3$), a consistent trend is observed. The onset and peak melting temperatures show minimal variation, suggesting that the introduction of EG does not significantly alter the initiation or intensity of the melting process. However, there is a gradual decrease in both measured and calculated latent heat values with an increasing percentage of EG. This indicates that the incorporation of EG influenced the latent heat characteristics of the composite, leading to a reduction in the amount of heat absorbed or released during the melting phase [30].

3.6. Thermal Conductivity

Thermal conductivity is critical factor influencing overall thermal behaviour of PCMs. While PCMs possess several desirable thermal properties, their low conductivity limits their conductive nature. TC of composite PCM samples was analysed with the help of Transient Hot Bridge (THB) technique. Ss-PCM samples impregnated with EG was tested for its thermal conductivity at a constant temperature of 20°C. For each sample, ten readings were taken to determine an average thermal conductivity value. Phonons are the main carriers of heat in graphite and other carbon materials. Fig. 8 (a) shows the schematic representation of thermal conductivity mechanism due to the formation of continuous graphitic networks that facilitate the phonon transport along the basal planes of graphite. Fig. 8 (b) demonstrates the outcomes of thermal conductivity values for the PCM and the EG-impregnated composite PCM (ss-PCM). As EG concentration amount enlarged upto 15 wt.%, TC of composite rises non-linearly, with values ranging from 0.212 to 1.01 W/m·K. {Fig. S3 (supplementary) showing the measurement principle of thermal conductivity through THB}.
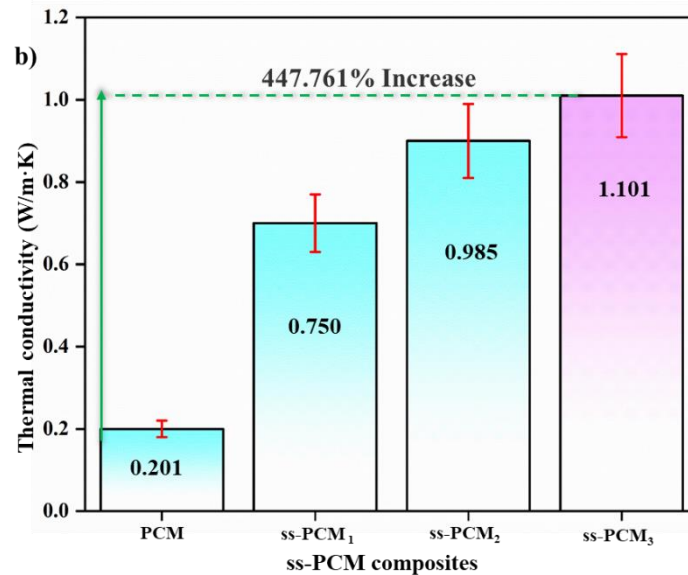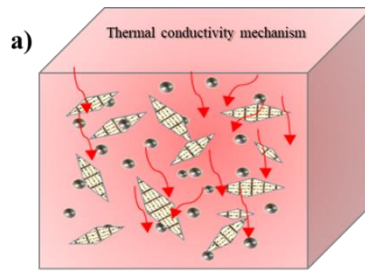
Fig. 8. a) Showing the mechanism of thermal conductivity in composite b) TC analysis of prepared ss-PCM composites consists of different weight% of EG

As per the findings, the thermal conductivity varies from 0.20 ± 0.020 W/m·K to 1.10 ± 0.110 W/m·K. The thermal conductivity for samples base PCM, ss-PCM$_1$, ss-PCM$_2$ and ss-PCM$_3$ are 0.20 ± 0.020 W/m·K, 0.750 ± 0.0750 W/m·K, 0.985 ± 0.0985 W/m·K and 1.101 ± 0.110 W/m·K respectively. The thermal conductivity of composite can also be influenced by the porosity, density, and morphology of the material. Improving organic PCM's thermal conductivity relies heavily on the creation of thermal networks, facilitating faster charging processes [62], [63]. During phase transition, thermal conductivity of ss-PCM composite can be attributed to phonon transfer through phonon vibration. The formation of well-established thermal networks leads to significant increase in thermal conductivity [64]. Selected EG possesses surface area of 500-1200 m^2/g, providing interconnected networks for efficient heat transfer pathways. It should be noted that higher concentrations can lead to non-uniform impregnation, which is undesirable as PCMs are favoured for their reliability during repeated thermal cycling between solid and liquid states. Additionally, the multiples of the test results in the supplementary file, which offers a detailed account of the measurement variability.
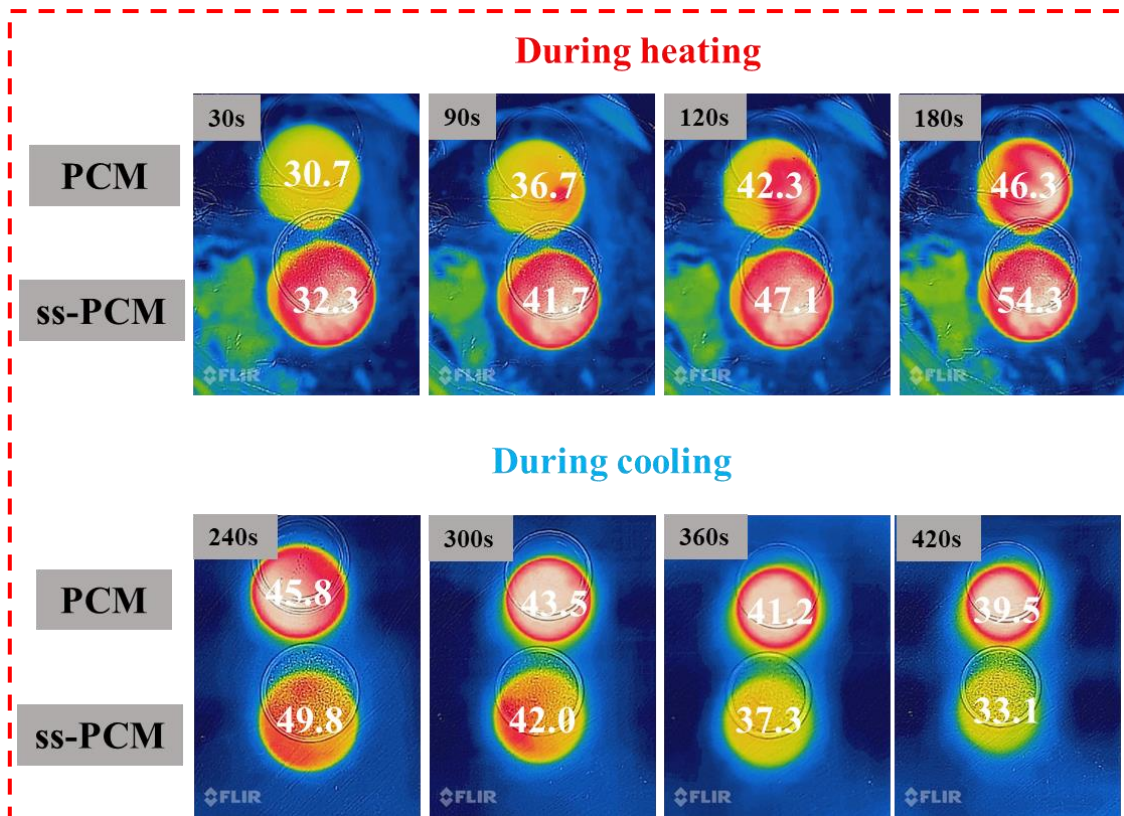
Fig. 9. Showing the comparison of heating and cooling process PCM and composites ss-PCMs

To visually represent the improved effect of thermal conductivity on the phase change material (PCM), a comprehensive study was conducted involving a comparison between the heating and cooling effects on pure PCM and ss-PCM. The specimens were subjected to heating on a controlled heating plate set at 60 ℃, with infrared thermal images captured after each 60-second interval. The comparison, as depicted in Fig. 9, reveals a striking difference in the heating and cooling behaviors between the composite ss-PCM and the base PCM PW-A46.

During the heating phase, the ss-PCM exhibits a notably faster temperature rise in contrast to the base PCM. This accelerated heating is attributed to the enhanced thermal conductivity facilitated by the composite structure. The incorporation of an EG matrix within the PCM contributes to improved heat transfer pathways, allowing for quicker thermal response. The efficiency of heat dissipation is further evident during the cooling phase, where the ss-PCM demonstrates a rapid decline in temperature compared to its counterpart, the base PW-A46.

The enhanced thermal conductivity observed in the ss-PCM is a result of the synergistic effect between the PCM and the thermally conductive EG matrix. This study provides a visual representation of the advantageous impact of improved thermal conductivity in the composite ss-PCM, offering insights into its potential applications where rapid and efficient thermal response is crucial.

3.6.1. Numerical model for heat transfer study using 2-D Energy simulation software.

A systematic, numerical study examines the heat transfer rate of base PW (organic-A46) PCM and ss-PCM$_3$ composites under various heat input circumstances, as seen in Fig. 10. A two-dimensional enclosure is investigated to exhibit PW-A46 thermal heat transfer rate by including porous additive EG as supporting material. In this investigation, the heat transfer from a heat source at 55 °C and 65 °C to a cold source at 0 °C has been calculated. The heat source is regulated to distinct variant temperatures of 55 °C and 65 °C, higher than the phase transition temperature (>46 °C) of the EG dispersed ss-PCM composites. The numerical investigation concentrates on the PW-A46 and EG encapsulated PCM composites 2D enclosures at a room temperature of 30 °C. Fig. 10 (a) represents the PW-A46 PCM 2D enclosure with a thermal conductivity of 0.201 W/(m·K), and Fig. 10 (b) shows the ss-PCM$_3$ 2D enclosure with a thermal conductivity of 1.10 W/(m·K). Both enclosures are of uniform length, 20 cm, and 10 cm width. It was suggested that the complete area of the energy storage unit was subjected to thermal energy from some heating source, sustaining unchange thermal energy. In addition, the selection of heat source temperatures at 55 °C and 65 °C is likely based on optimizing the dispersed EG base ss-PCM. These temperatures correspond to the phase transition temperature higher than the melting point of the PCM, guaranteeing adequate energy storage and release. The selection is probably based on thermodynamic considerations to optimize the material's ability to absorb and release heat within a feasible temperature range for the intended use.

Case 1. Heat transfer analysis of base (A-46) PCM.

Case 2. Heat transfer analysis of A-46 + 15EG composite (ss-PCM₃)

*All dimensions are in mm.
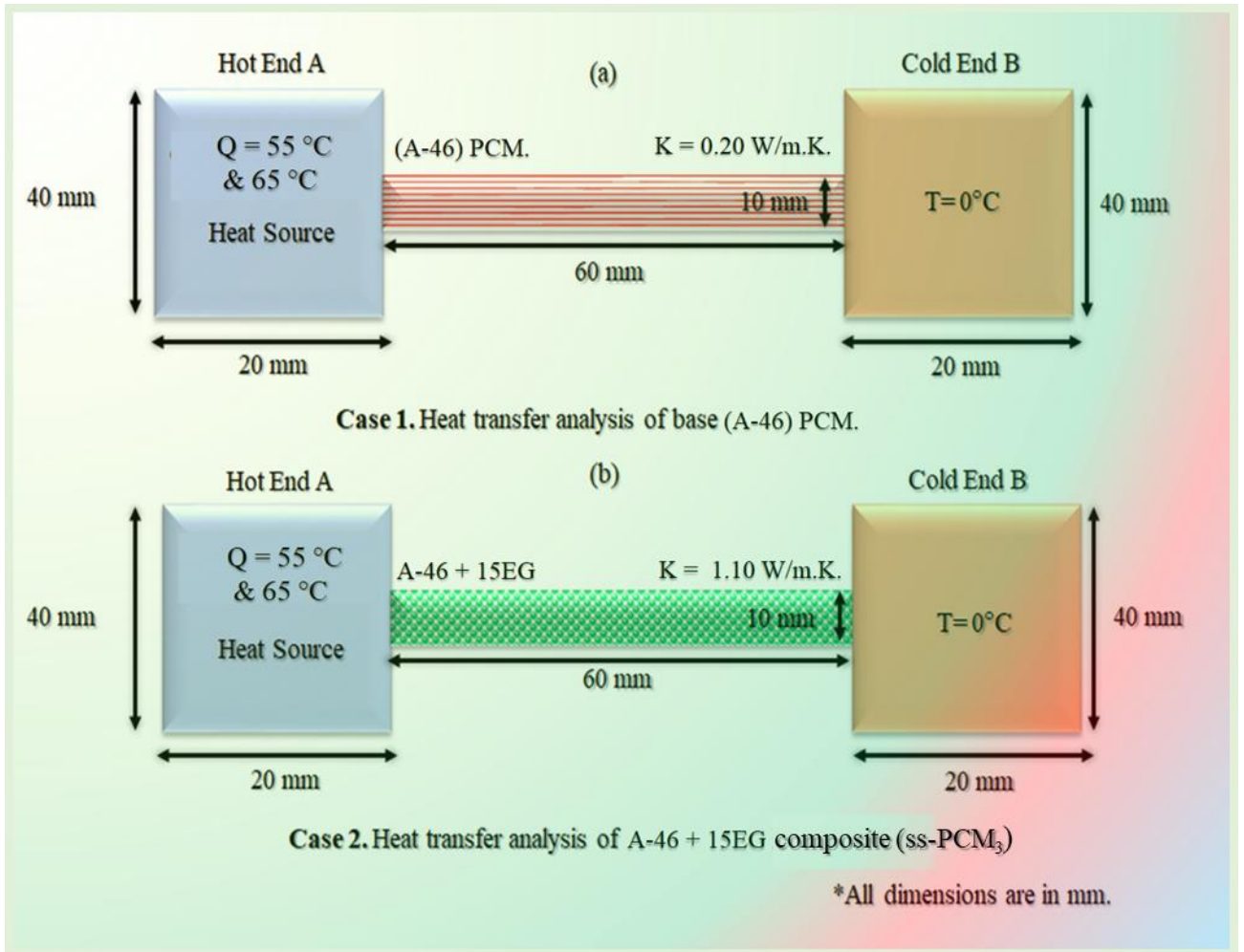
Fig. 10. Illustration of problem under analysis (a) base PCM (PW-A46); and (b) ss-PCM composite

3.6.2. Thermal performance assessment of PCMs and composite ss-PCM for energy storage in varied energy input environments

After examining the experimental characterisation results described above, the PW-A46 PCM with a 15 wt% EG base exhibits a higher thermal conductivity. This work utilises numerical analysis to explore the energy storage capacities of the PW-A46 PCM layer and ss-PCM$_3$ by examining their heat transfer performance. The present study uses 2-D energy software to understand the heat transfer rate of EG-PW based ss-PCM composite and the base (PW-A46) PCM. The input parameters such as thermal conductivity, environmental temperature, sample temperature, absorptivity, transmissivity, specific heat, density, and external heat source temperature are feeders in 2-D energy software to observe the temperature distribution of the base PW-A46 and ss-PCM$_3$ composite to understand the heat transfer rate. The primary focus is transferring thermal energy from end A to end B through the composite and the base PCM between both ends. Herein, end A is considered a heat

590   source, and end B indicates the heat transfer rate through the base PCM and the composite.

591   The heat input source exhibits a varied temperature range of 55 °C and 65 °C. Specifically,

592   heat transfer from end A is (a) case 1 (55 °C) and (b) case 2 (65 °C), while end B is initially

593   set at 0 °C. Fig. 11 and Fig. 12 display the heat transfer rate of base PCM and composite

594   within a two-dimensional enclosure featuring contour plots. In this context, a simulation

595   analysis for steady-state heat transfer is conducted, with the heat sink consistently held at a

596   constant temperature throughout all the discussed cases. Based on Fig. 11 and Fig. 12, with

597   an increase in heat supply temperature from the source (end A), the results show that the

598   maximum possible heat transfer penetration through the ss-PCM$_3$ composite reaching the

599   end B is improved considerably, as compared to the base PCM. The superior heat transfer

600   in ss-PCM$_3$ composite, compared to the base PCM, is attributed to the inclusion of

601   conductive elements, facilitating the thermal networks enhancing thermal conductivity and

602   facilitating more efficient heat propagation, resulting in improved penetration to end B.

603   Similarly, the contour plots provide an effective means to comprehend the role of thermal

604   conductivity in enhancing the energy charging rate. Noteworthy observations include a) an

605   augmented energy transfer penetration in the ss-PCM$_3$ composite compared to the base

606   PCM, attributed to heightened thermal conductivity; and b) an increase in the magnitude of

607   thermal energy, well-illustrated by the temperature values at end point B. Fig. 11 and 12

608   distinctly present 2D enclosures of the base PCM and ss-PCM3 composite under diverse

609   heat sources at various time intervals. (Please see the videos (V1 and V2) attached with the

610   supplementary document under section S4. For a better understanding of heat transfer

611   analysis (thermal conductivity) of base (PCM) and ss-PCM$_3$ at heat input source of Q= 55

612   °C and Q= 65 °C).
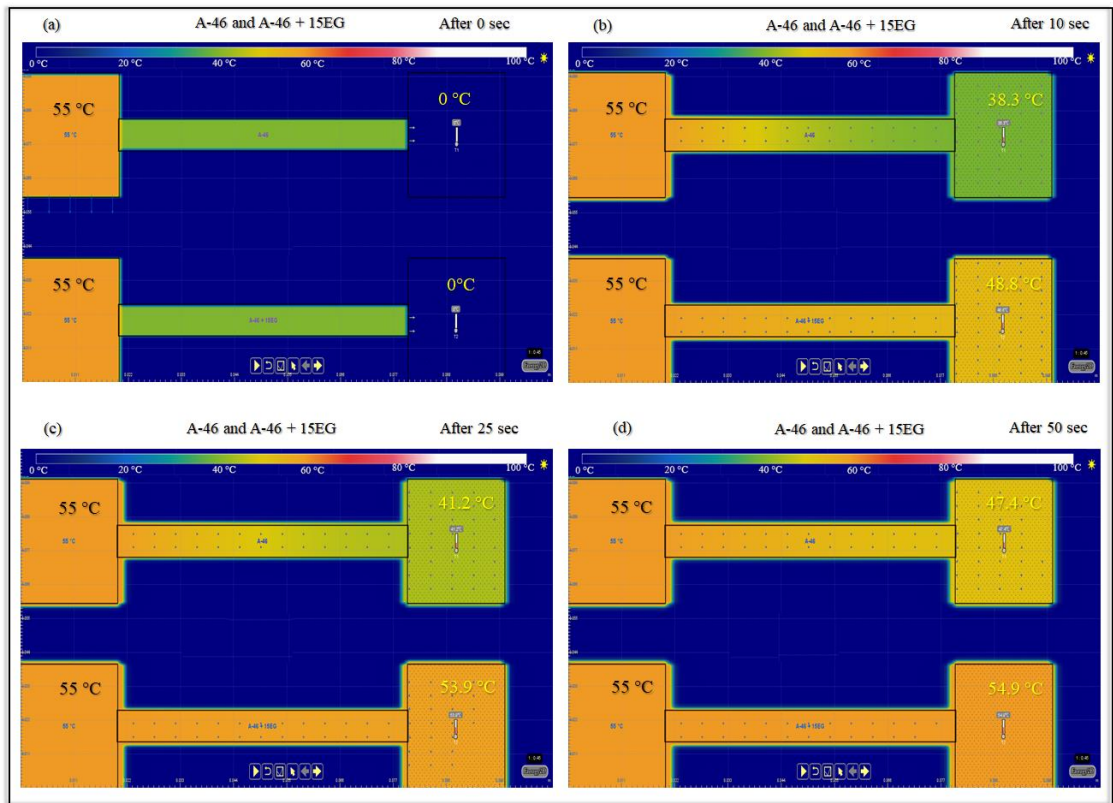
Fig. 11 Illustrates the thermal distribution (temperature contours) of the base PCM and ss-PCM3 composite under a 55 °C input heat source for different time intervals: (a) 0 seconds, (b) PCM at 10 seconds, (c) 30 seconds, and (d) 60 seconds.

3.7. Leakage test

To test leakage resistance of the PCM samples, a detailed and careful procedure was followed. These samples were compressed into uniform round blocks measuring 30mm x 10mm. These blocks were then placed on filter papers to assess any possible leakage during thermal treatment. Treatment was conducted at controlled temperature of 60°C, ˜15 °C above melting point of PCM [19]. The samples were exposed to this temperature for 45 minutes to simulate long-term exposure and assess the PCM's stability. After the thermal treatment, the samples were carefully removed from the filter papers and visually inspected for any signs of leakage, which might indicate a compromise of the encapsulation integrity.

Table 5 PCM and ss-PCM weight loss measurements after leakage tests

| Time (mins)	Weight loss (mg)			
	PCM	ss-PCM$_1$	ss-PCM$_2$	ss-PCM$_3$
0	1400	1400	1400	1400
15	658	1210	1281	1395
30	0 (27 mins)	1087	1197	1394
45	0	965	1133	1394

Table 5 presents the weight loss measurements for both the base PCM and the ss-PCM at various time intervals during leakage tests. The initial weight for both PCM and ss-PCM is consistent at 1400 mg. As the test progresses, the weight loss is recorded, reflecting the extent of material leakage. Notably, after 15 minutes, the PCM registers a substantial weight loss of 658 mg, while the ss-PCM variants (ss-PCM$_1$, ss-PCM$_2$, and ss-PCM$_3$) show varying degrees of weight loss (1210 mg, 1281 mg, and 1395 mg, respectively). Intriguingly, after 30 minutes, the PCM weight loss reaches 0, indicating a potential sealing effect after 27 minutes, while the ss-PCM variants continue to exhibit weight loss. The subsequent entries at 45 minutes reinforce the stability of PCM with no further weight loss, contrasting with ongoing weight reductions in the ss-PCM variants. These measurements underscore the leakage resistance of the base PCM compared to the ss-PCM variants under the given test conditions.

During the observation, it was noted that the ss-PCM$_1$ sample exhibited noticeable leakage, while the ss-PCM$_2$ sample showed minimal leakage due to the accumulation of excess PCM on the surface. However, after conducting surface treatment by removing the PCM from the composite surface, no leakage was observed. Furthermore, the ss-PCM$_3$ sample exhibited no leakage at all, indicating that all the PCM had been absorbed by the EG. The absence of any

leakage in the ss-PCM₃ sample can be attributed to the complete absorption of PCM by EG. During the vacuum impregnation process, the PCM is thoroughly disseminated and integrated into EG having porous structure, ensuring that there are no voids or gaps through which the PCM could potentially escape.
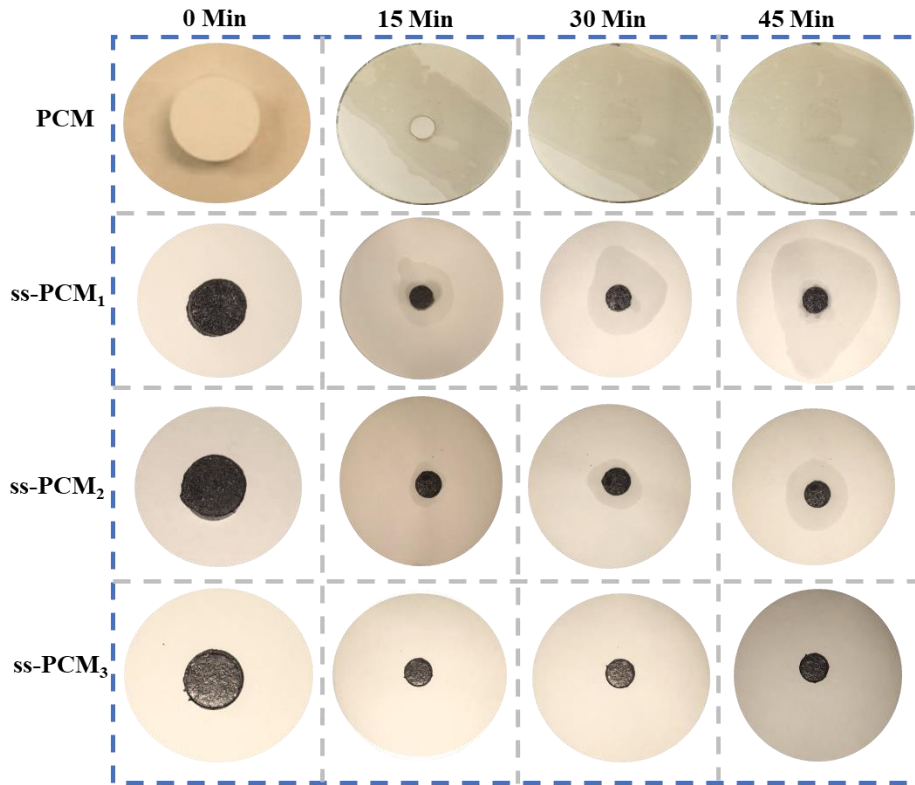

Fig. 13. Leakage test results

The unique porous nature of EG provides an excellent matrix for the PCM to be uniformly distributed and absorbed within its structure. The weight reduce in ss-PCM₃ sample was found to be negligible, which was ensured by measuring the weight of ss-PCM composites before and after the leakage test. The leakage test results are illustrated as in Fig. 13. Based on these findings, it can be concluded that the addition of 15% EG (ss-PCM₃) is considered optimal in this composite sample. This concentration effectively minimizes leakage while maintaining desirable thermal conductivity properties.

4. Thermal cycling analysis

To verify long-term operation of ss-PCM₃ composite, thermal cycling test was conducted. The test involved subjecting pure PW-A46 PCM and EG dispersed composite ss-PCM₃ to 500 cycles of heating and cooling using a customized thermal cycler machine. SEM analysis as shown in Fig. 14 (a, b) confirmed presence of consistent scattering of PW-A46 PCM within the EG matrix, without any chemical reactions involving PCM molecules. The homogeneously

dispersed PCM within the porous EG network as shown in Fig. 10 (b) played a crucial role in enhancing thermal properties by providing efficient thermal networks and preventing agglomeration. FTIR analysis Fig. 14 (c) indicated possible chemical interactions and stability of both base PCM and composite PCM, as evidenced by similarity in vibration peaks to pre-cycling state. The absence of peak shifts after 500 thermal cycles indicated the preservation of electronic distribution and hybridization. These results suggest that the ss-PCM$_3$ composite exhibits robust thermal stability, making it a promising choice for real-time applications. Furthermore, Fig. 14 (d) provides visual evidence of PCM composites before and after undergoing 500 heating-cooling cycles, allowing readers to observe the changes directly.
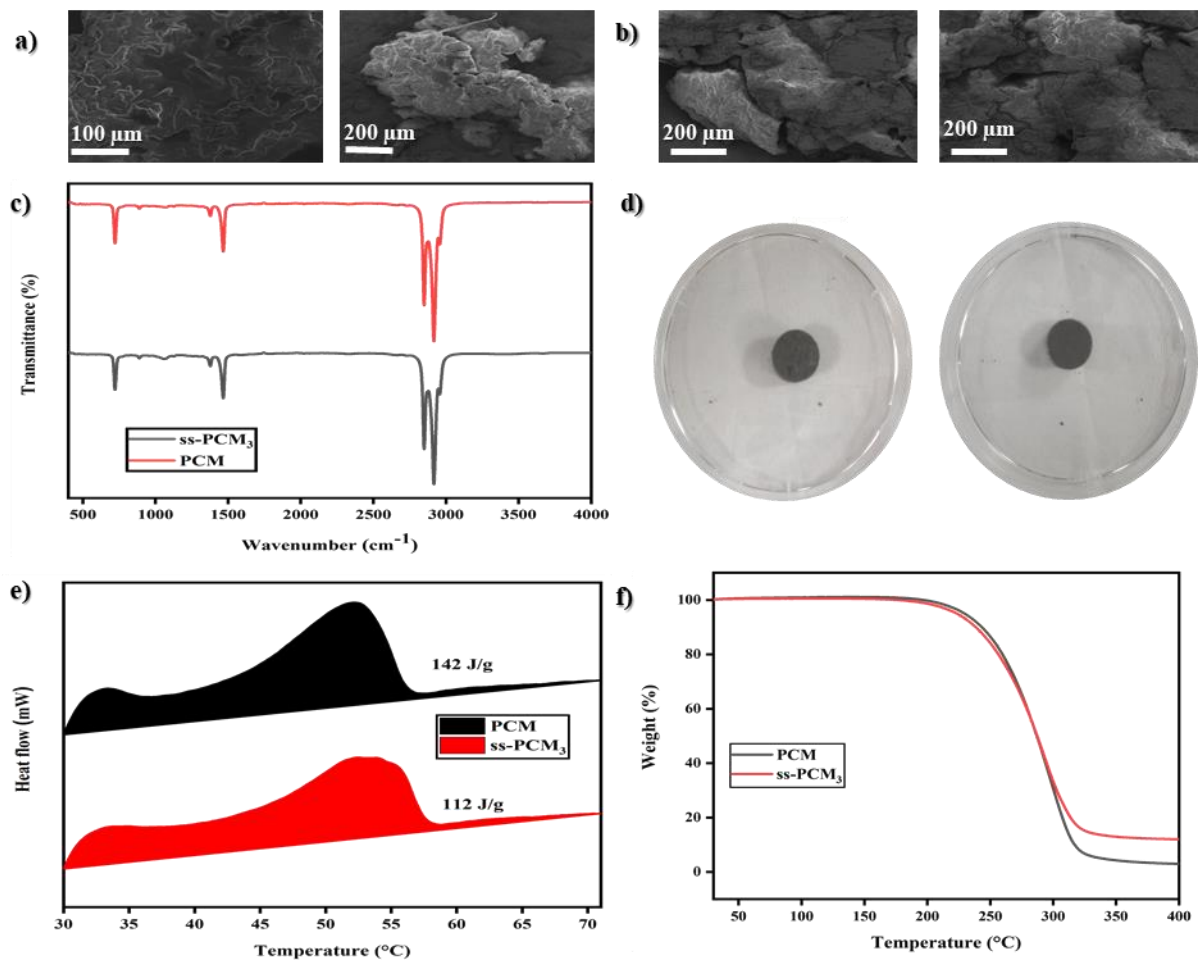
Fig. 14. 500 Heating cooling cycling analysis. (a) PW-A46 PCM Microstructure image, (b) PW-A46 15%EG PCM SEM image, (c) Functional group analysis, (d) photograph of composite PCM prior and subsequent 500 heating cooling cycles, (e) latent heat through DSC (f) TGA analysis

Fig. 14 (e) displays phase transition temperature and melting enthalpy variations of both base PCM and composite PCM after thermal cycle testing. Improper crystallization during phase

30

transitions causes shifts in phase transition temperatures, which in turn modifies other thermophysical parameters of composite PCM samples. Fig. 14 (f) provides insights into thermal stability of PCM, illustrating presence of volatile components and weight loss percentage with increasing temperature. The composite PCM shows an increase in decomposition temperature after 500 thermal cycles, indicating improved thermal stability due to repeated temperature changes. These observations suggest role of ambient conditions and temperature effects on the behaviour of PCMs during DSC testing [65].

5. Electrical-to-thermal energy conversion

The verification of the electrical characteristics of developed ss-PCM was achieved by demonstrating their ability to transmit electricity to light emitting diode, as illustrated in Fig. 15. Upon activation of the power source, the bright diode exhibited illumination when it was connected to power source through the ss-PCM and copper wire. The findings of this study indicate that the produced ss-PCM exhibited exceptional electrical conductivity. This can be related to the existence of a three-dimensional ceaseless conductive matrix arrangement of encapsulating EG framework.
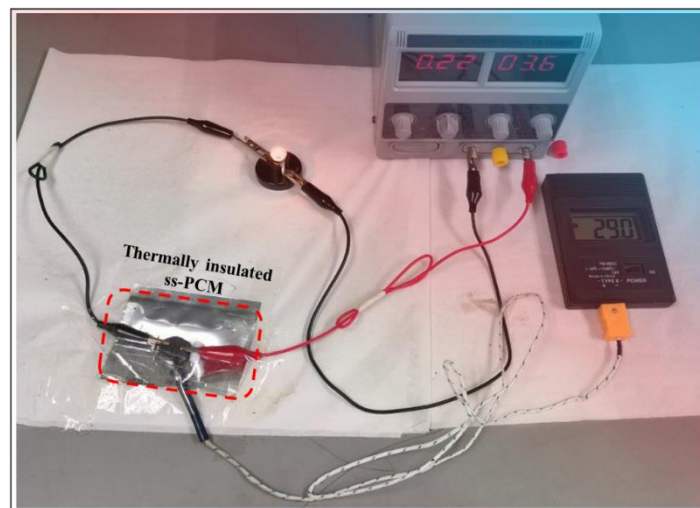

Fig. 15. Diode coupled to an ss-PCM (PW/EG) generating light.

In addition, an assessment was conducted on electric-to-thermal energy conversion and storage capability of the prepared ss-PCM. The experimental arrangement is depicted in Fig. 16 (a). According to Joule's law, the generation of heat flow can be attributed to the passage of an electric current through a conductor, where the heat generated (Q) is directly proportional to the square of the current (I), the resistance (R) of the conductor, and the time (T) during which the current flows, i.e., $Q = I^2RT$ [66], [67]. Upon activation of the power source, the device

713 would provide a pathway for conducting electricity. Subsequently, ss-PCM system would

714 proceed to accumulate and retain thermal energy produced by the flow of electric current. Fig.

715 16 (b) presents the temperature-time curve of composite PW/EG ss-PCM. A melting plateau

716 was observed in the temperature range of around 42 to 51 °C. This indicates successful

717 optimization of the experimental conditions to achieve the desired temperature stability during

718 the phase transition, which signifies the conversion and storage of electric energy into thermal

719 energy in the ss-PCM system, akin to the light-to-thermal energy conversion process. After the

720 power was switched off, there was a sudden decrease in temperature until it reached a stable

721 level at approximately 42 °C. This plateau persisted for approximately 20 minutes, indicating

722 the release of stored heat. The electrical-to-thermal energy conversion efficiency (φ) of

723 developed ss-PCM has been determined using Equation (3) [45].

$$\varphi = \frac{m\Delta H}{UI_e t} \dots \dots \dots (3).$$

725 The variables m represents the weight while ΔH denotes heating enthalpy of ss-PCM

726 respectively. I_e represents the electric current flowing through the conducting circuit, U denotes

727 voltage applied, whereas t signifies the elapsed time.

728
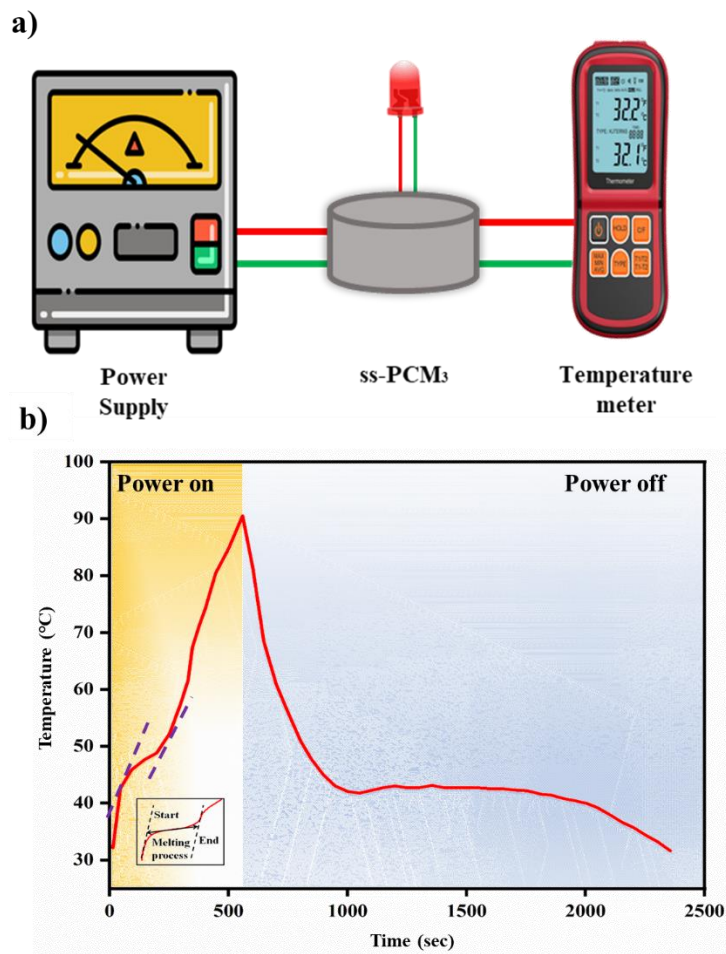
Fig. 16. (a) Experimental setup for assessing the device's electro-to-thermal conversion. (b) The on/off power operation temperature fluctuation curve of the generated solid-state phase transition material (PW/EG) is shown.

The electrical-to-thermal efficiency of the ss-PCM composite was assessed using a voltage of 4.8 volts. The experimental setup involved subjecting the composite to electric load under controlled laboratory conditions. Temperature changes were monitored using thermocouples and recorded with a data acquisition system. The tangential method was applied to the t-axis (time) of the inset of Fig. 16 (b) to identify the starting and terminating points of the phase change, crucial for efficiency calculations. The latent heat released or absorbed during the phase change was determined based on temperature changes. The electro-to-thermal efficiency was then calculated using the obtained latent heat values. The electrical-to-thermal energy conversion efficiency (φ) of developed ss-PCM$_3$ has determined to be 61.89%. This observation indicates that the developed PCM composites had remarkable thermal storage capacity, enabling them to effectively retain heat within the operational electric circuit even at lower temperatures.

6. Conclusion

This study aimed to comprehensively investigate the thermophysical characteristics and electrical-to-thermal conversion capabilities of shape-stable phase change materials (PCMs) fabricated through vacuum impregnation of EG (expanded graphite) into an PW-A46 organic PCM matrix. The innovative approach of utilizing vacuum impregnation sought to enhance the material's overall performance and suitability for various applications requiring efficient thermal management. The key findings of this study are as follows:

- SEM analysis revealed a homogeneous distribution of PCM within the EG matrix, establishing effective thermal networks conducive to enhanced heat transfer.
- Optimal chemical and thermal stability were observed at a weight concentration of 15%, showcasing the efficacy of the fabrication process.
- The incorporation of EG led to an impressive 447% increase in thermal conductivity, reaching 1.101 W/m·K, albeit with a marginal reduction of approximately 13.83% in latent heat.
- Thermal gravimetric analyses (TGA) demonstrated superior breakdown temperatures compared to base PCMs, indicating enhanced thermal stability.
- Fourier-transform infrared spectroscopy (FTIR) confirmed the chemical stability of the composite PCM even after 500 heating-cooling cycles, underlining its durability.

33

- Thermal cycling tests indicated heightened decomposition points while maintaining consistent latent enthalpy values, affirming the material's resilience under repeated thermal stresses.

- The resultant composite PCM exhibited a remarkable 61.89% efficiency in converting electrical energy to thermal energy, showcasing its potential for applications in electronic components and battery temperature management.

However, certain constraints need acknowledgment. The experiments, conducted in a controlled laboratory setting, may limit the generalization of results to real-world scenarios with varying environmental conditions. Flammability remains untested, necessitating further investigation for a comprehensive safety evaluation. Furthermore, additional research on the mechanical characteristics and elasticity of the composite material is imperative for its diverse applications. Overall, the findings underscore the promising potential of the fabricated PCM composite for advancing thermal management technologies.

Acknowledgments

Declaration-of-interests: It is declared by the authors that they do not have any known personal relationships or competing financial interests that may have influenced described work presented in this research paper.

References

[1] J. Jeon, J. H. Lee, J. Seo, S. G. Jeong, and S. Kim, "Application of PCM thermal energy storage system to reduce building energy consumption," *J Therm Anal Calorim*, vol. 111, no. 1, pp. 279–288, 2013, doi: 10.1007/S10973-012-2291-9.

[2] Y. A. Bhutto, A. K. Pandey, R. Saidur, K. Sharma, and V. V. Tyagi, "Critical insights and recent updates on passive battery thermal management system integrated with nano-enhanced phase change materials," *Materials Today Sustainability*, vol. 23, p. 100443, Sep. 2023, doi: 10.1016/j.mtsust.2023.100443.

[3] K. Venkateswarlu and K. Ramakrishna, "Recent advances in phase change materials for thermal energy storage-a review," *Journal of the Brazilian Society of Mechanical Sciences and Engineering 2021 44:1*, vol. 44, no. 1, pp. 1–17, Dec. 2021, doi: 10.1007/S40430-021-03308-7.

[4] M. Mubarrat, M. M. Mashfy, T. Farhan, and M. M. Ehsan, "Research Advancement and Potential Prospects of Thermal Energy Storage in Concentrated Solar Power Application," *International Journal of Thermofluids*, vol. 20, p. 100431, Nov. 2023, doi: 10.1016/j.ijft.2023.100431.

[5] G. Simonsen, R. Ravotti, P. O'Neill, and A. Stamatiou, "Biobased phase change materials in energy storage and thermal management technologies," *Renewable and Sustainable Energy Reviews*, vol. 184, p. 113546, Sep. 2023, doi: 10.1016/j.rser.2023.113546.

[6] A. S. Fleischer, "Types of PCMs and their selection," *SpringerBriefs in Applied Sciences and Technology*, no. 9783319209210, pp. 37–47, 2015, doi: 10.1007/978-3-319-20922-7_3/COVER.

[7] H. Ji *et al.*, "Enhanced thermal conductivity of phase change materials with ultrathin-graphite foams for thermal energy storage," *Energy Environ. Sci.*, vol. 7, no. 3, pp. 1185–1192, 2014, doi: 10.1039/C3EE42573H.

[8] D.-L. Han *et al.*, "Thermally conductive composite phase change materials with excellent thermal management capability for electronic devices," *Journal of Materials Science: Materials in Electronics*, vol. 33, no. 2, pp. 1008–1020, Jan. 2022, doi: 10.1007/s10854-021-07371-7.

[9] H. Tafrishi, S. Sadeghzadeh, and R. Ahmadi, "Molecular dynamics simulations of phase change materials for thermal energy storage: a review," 2022, doi: 10.1039/d2ra02183h.

[10] F. Hanif *et al.*, "Form-Stable Phase Change Material with Wood-Based Materials as Support," *Polymers 2023, Vol. 15, Page 942*, vol. 15, no. 4, p. 942, Feb. 2023, doi: 10.3390/POLYM15040942.

[11] F. Marske, J. Martins De Souza E Silva, R. B. Wehrspohn, T. Hahn, and D. Enke, "Synthesis of monolithic shape-stabilized phase change materials with high mechanical stability via a porogen-assisted in situ sol–gel process," *RSC Adv*, vol. 10, no. 6, pp. 3072–3083, Jan. 2020, doi: 10.1039/C9RA10631F.

[12] W. Luo *et al.*, "Lipophilic Modified Hierarchical Multiporous rGO Aerogel-Based Organic Phase Change Materials for Effective Thermal Energy Storage," *ACS Appl Mater Interfaces*, vol. 14, no. 49, pp. 55098–55108, Dec. 2022, doi: 10.1021/acsami.2c17041.

[13] J. Li, X. Hu, C. Zhang, W. Luo, and X. Jiang, "Enhanced thermal performance of phase-change materials supported by mesoporous silica modified with polydopamine/nano-metal particles for thermal energy storage," *Renew Energy*, vol. 178, pp. 118–127, Nov. 2021, doi: 10.1016/j.renene.2021.06.021.

[14] A. Trigui, M. Abdelmouleh, and C. Boudaya, "Performance enhancement of a thermal energy storage system using shape-stabilized LDPE/hexadecane/SEBS composite PCMs by copper oxide addition," *RSC Adv*, vol. 12, no. 34, pp. 21990–22003, Aug. 2022, doi: 10.1039/D2RA02437C.

[15] Jaspreet Singh Aulakh and P. J. Deepika, "Development of Paraffin-Based Shape-Stable Phase Change Material for Thermal Energy Storage," *Polymer Science - Series A*, vol. 64, no. 4, pp. 308–317, Aug. 2022, doi: 10.1134/S0965545X22200056/METRICS.

[16] F. Samani, A. R. Bahramian, and A. Sharif, "Shape-stable phenolic/polyethylene glycol phase change material: kinetics study and improvements in thermal properties of nanocomposites," *Iranian Polymer Journal (English Edition)*, vol. 27, no. 7, pp. 495–505, Jul. 2018, doi: 10.1007/S13726-018-0626-5/METRICS.

[17] Y. Ma *et al.*, "A structured phase change material integrated by MXene/AgNWs modified dual-network and polyethylene glycol for energy storage and thermal management," *Appl Energy*, vol. 349, p. 121658, Nov. 2023, doi: 10.1016/j.apenergy.2023.121658.

[18]   S. Guo *et al.*, "Shape-stabilized phase change materials based on superhydrophobic polymethylsilsesquioxane aerogels with extremely high paraffin loading for energy storage," *Journal of Porous Materials*, vol. 28, no. 2, pp. 345–354, Apr. 2021, doi: 10.1007/S10934-020-00997-8/METRICS.

[19]   Y. Xie *et al.*, "Paraffin/polyethylene/graphite composite phase change materials with enhanced thermal conductivity and leakage-proof," *Adv Compos Hybrid Mater*, vol. 4, no. 3, pp. 543–551, Sep. 2021, doi: 10.1007/S42114-021-00249-6/METRICS.

[20]   L. Luo *et al.*, "Form-stable phase change materials based on graphene-doped PVA aerogel achieving effective solar energy photothermal conversion and storage," *Solar Energy*, vol. 255, pp. –156, May 2023, doi: 10.1016/j.solener.2023.03.037.

[21]   M. Senthilkumar, K. R. Balasubramanian, R. K. Kottala, S. P. Sivapirakasam, and L. Maheswari, "Characterization of form-stable phase-change material for solar photovoltaic cooling," *J Therm Anal Calorim*, vol. 141, no. 6, pp. 2487–2496, Sep. 2020, doi: 10.1007/S10973-020-09521-1/METRICS.

[22]   Y. Wang *et al.*, "Shape-stable and fire-resistant hybrid phase change materials with enhanced thermoconductivity for battery cooling," *Chemical Engineering Journal*, vol. 431, p. 133983, Mar. 2022, doi: 10.1016/j.cej.2021.133983.

[23]   Z. Ling, S. Li, Z. Zhang, X. Fang, X. Gao, and T. Xu, "A shape-stabilized MgCl2·6H2O–Mg(NO3)2·6H2O/expanded graphite composite phase change material with high thermal conductivity and stability," *J Appl Electrochem*, vol. 48, no. 10, pp. 1131–1138, Oct. 2018, doi: 10.1007/S10800-018-1223-1/METRICS.

[24]   Z. J. Duan *et al.*, "CaCl2·6H2O/Expanded graphite composite as form-stable phase change materials for thermal energy storage," *J Therm Anal Calorim*, vol. 115, no. 1, pp. 111–117, Jan. 2014, doi: 10.1007/S10973-013-3311-0/METRICS.

[25]   P. K. S. Rathore and S. kumar Shukla, "Improvement in thermal properties of PCM/Expanded vermiculite/expanded graphite shape stabilized composite PCM for building energy applications," *Renew Energy*, vol. 176, pp. 295–304, Oct. 2021, doi: 10.1016/j.renene.2021.05.068.

[26]   T. Wang, K. Wang, F. Ye, Y. Ren, and C. Xu, "Characterization and thermal properties of a shape-stable Na2CO3-K2CO3/coal fly ash/expanded graphite composite phase change materials for high-temperature thermal energy storage," *J Energy Storage*, vol. 33, Jan. 2021, doi: 10.1016/j.est.2020.102123.

[27]   X. Zhao, K. Lei, S. Wang, B. Wang, L. Huang, and D. Zou, "A shape-memory, room-temperature flexible phase change material based on PA/TPEE/EG for battery thermal management," *Chemical Engineering Journal*, vol. 463, p. 142514, May 2023, doi: 10.1016/j.cej.2023.142514.

[28]   T. Shi *et al.*, "Preparation and characterization of composite phase change materials based on paraffin and carbon foams derived from starch," *Polymer (Guildf)*, vol. 212, p. 123143, Jan. 2021, doi: 10.1016/j.polymer.2020.123143.

[29]   B. Tian *et al.*, "Synergistic enhancement of thermal conductivity for expanded graphite and carbon fiber in paraffin/EVA form-stable phase change materials," *Solar Energy*, vol. 127, pp. 48–55, Apr. 2016, doi: 10.1016/j.solener.2016.01.011.

[30]   K. Balasubramanian, A. Kumar Pandey, R. Abolhassani, H.-G. Rubahn, S. Rahman, and Y. Kumar Mishra, "Tetrapods based engineering of organic phase change material for thermal energy storage," *Chemical Engineering Journal*, vol. 462, p. 141984, Apr. 2023, doi: 10.1016/j.cej.2023.141984.

[31] X. Hu *et al.*, "Upgrading Electricity Generation and Electromagnetic Interference Shielding Efficiency via Phase-Change Feedback and Simple Origami Strategy," *Advanced Science*, vol. 10, no. 14, May 2023, doi: 10.1002/advs.202206835.

[32] X. Li *et al.*, "Wearable Janus-Type Film with Integrated All-Season Active/Passive Thermal Management, Thermal Camouflage, and Ultra-High Electromagnetic Shielding Efficiency Tunable by Origami Process," *Adv Funct Mater*, vol. 33, no. 18, May 2023, doi: 10.1002/adfm.202212776.

[33] S. Gong *et al.*, "A Multifunctional Flexible Composite Film with Excellent Multi-Source Driven Thermal Management, Electromagnetic Interference Shielding, and Fire Safety Performance, Inspired by a 'Brick–Mortar' Sandwich Structure," *Adv Funct Mater*, vol. 32, no. 26, Jun. 2022, doi: 10.1002/adfm.202200570.

[34] G. Hekimoğlu, A. Sarı, O. Gencel, V. V. Tyagi, and R. K. Sharma, "Activated carbon/expanded graphite hybrid structure for development of nonadecane based composite PCM with excellent shape stability, enhanced thermal conductivity and heat charging-discharging performance," *Thermal Science and Engineering Progress*, vol. 44, p. 102081, Sep. 2023, doi: 10.1016/j.tsep.2023.102081.

[35] H. Pan, T. Li, L. Xu, K. Li, and Y. Shen, "Shape-stable composite phase change materials encapsulated by lignin-based ordered porous carbon for thermal energy storage," *Journal of Wood Chemistry and Technology*, vol. 43, no. 2, pp. 92–102, Mar. 2023, doi: 10.1080/02773813.2023.2187063.

[36] S. Wu *et al.*, "Preparation and properties of shape-stable phase change material with enhanced thermal conductivity based on SiC porous ceramic carrier made of iron tailings," *Appl Energy*, vol. 355, p. 122256, Feb. 2024, doi: 10.1016/j.apenergy.2023.122256.

[37] A. P. Tetuko *et al.*, "Encapsulation of paraffin-magnetite, paraffin, and polyethylene glycol in concretes as thermal energy storage," *J Energy Storage*, vol. 68, p. 107684, Sep. 2023, doi: 10.1016/J.EST.2023.107684.

[38] X. Zuo, X. Zhao, J. Li, Y. Hu, H. Yang, and D. Chen, "Enhanced thermal conductivity of form-stable composite phase-change materials with graphite hybridizing expanded perlite/paraffin," *Solar Energy*, vol. 209, pp. 85–95, Oct. 2020, doi: 10.1016/J.SOLENER.2020.08.082.

[39] T. Li *et al.*, "Form-stable phase change composites with multistage pores based on black phosphorus nanosheets/PVA aerogel for efficient solar photothermal conversion," *Materials Today Sustainability*, vol. 25, p. 100611, Mar. 2024, doi: 10.1016/j.mtsust.2023.100611.

[40] B. Hou, H. Sun, T. Peng, X. Zhang, and Y. Ren, "Rapid preparation of expanded graphite at low temperature," *New Carbon Materials*, vol. 35, no. 3, pp. 262–268, Jun. 2020, doi: 10.1016/S1872-5805(20)60488-7.

[41] X. Pang, Y. Xin, X. Shi, and J. Xu, "Effect of different size-modified expandable graphite and ammonium polyphosphate on the flame retardancy, thermal stability, physical, and mechanical properties of rigid polyurethane foam," *Polym Eng Sci*, vol. 59, no. 7, pp. 1381–1394, Jul. 2019, doi: 10.1002/pen.25123.

[42] K. Chun, J. Kim, and D. Rie, "Thermal Characteristics of Expandable Graphite–Wood Particle Composites," *Materials*, vol. 13, no. 12, p. 2732, Jun. 2020, doi: 10.3390/ma13122732.

[43]   X. K. Yu and Y. B. Tao, "Preparation and characterization of paraffin/expanded graphite composite phase change materials with high thermal conductivity," *Int J Heat Mass Transf*, vol. 198, p. 123433, Dec. 2022, doi: 10.1016/j.ijheatmasstransfer.2022.123433.

[44]   G. Zhang, Y. Sun, C. Wu, X. Yan, W. Zhao, and C. Peng, "Low-cost and highly thermally conductive lauric acid–paraffin–expanded graphite multifunctional composite phase change materials for quenching thermal runaway of lithium-ion battery," *Energy Reports*, vol. 9, pp. 2538–2547, Dec. 2023, doi: 10.1016/j.egyr.2023.01.102.

[45]   W. Wu, X. Huang, K. Li, R. Yao, R. Chen, and R. Zou, "A functional form-stable phase change composite with high efficiency electro-to-thermal energy conversion," *Appl Energy*, vol. 190, pp. 474–480, Mar. 2017, doi: 10.1016/j.apenergy.2016.12.159.

[46]   X. Li *et al.*, "Multifunctional HDPE/CNTs/PW composite phase change materials with excellent thermal and electrical conductivities," *J Mater Sci Technol*, vol. 86, pp. 171–179, Sep. 2021, doi: 10.1016/j.jmst.2021.02.009.

[47]   "1.3: Measurements, Uncertainty and Significant Figures - Physics LibreTexts." Accessed: Nov. 07, 2023. [Online]. Available: https://phys.libretexts.org/Courses/Georgia_State_University/GSU-TM-Physics_I_%282211%29/01%3A_Introduction_to_Physics_and_Measurements/1.03%3A_Measurements_Uncertainty_and_Significant_Figures

[48]   A. K. Hassan, J. Abdulateef, M. S. Mahdi, and A. F. Hasan, "Experimental evaluation of thermal performance of two different finned latent heat storage systems," *Case Studies in Thermal Engineering*, vol. 21, Oct. 2020, doi: 10.1016/J.CSITE.2020.100675.

[49]   G. Fang, Z. Chen, and H. Li, "Synthesis and properties of microencapsulated paraffin composites with SiO2 shell as thermal energy storage materials," *Chemical Engineering Journal*, vol. 163, no. 1–2, pp. 154–159, Sep. 2010, doi: 10.1016/J.CEJ.2010.07.054.

[50]   S. Ramakrishnan, X. Wang, J. Sanjayan, E. Petinakis, and J. Wilson, "Development of thermal energy storage cementitious composites (TESC) containing a novel paraffin/hydrophobic expanded perlite composite phase change material," *Solar Energy*, vol. 158, pp. 626–635, Dec. 2017, doi: 10.1016/J.SOLENER.2017.09.064.

[51]   K. B *et al.*, "Synthesis and characterization of conducting Polyaniline@cobalt-Paraffin wax nanocomposite as nano-phase change material: Enhanced thermophysical properties," *Renew Energy*, vol. 173, pp. 1057–1069, Aug. 2021, doi: 10.1016/J.RENENE.2021.04.050.

[52]   Q. Wei *et al.*, "High-performance expanded graphite from flake graphite by microwave-assisted chemical intercalation process," *Journal of Industrial and Engineering Chemistry*, vol. 122, pp. 562–572, Jun. 2023, doi: 10.1016/j.jiec.2023.03.020.

[53]   L. Feng, J. Wu, W. Sun, and W. Cai, "Effects of Pore Structure and Pore Size of Expanded Graphite on the Properties of Paraffin Wax/Expanded Graphite Composite Phase Change Materials," *Energies (Basel)*, vol. 15, no. 12, p. 4201, Jun. 2022, doi: 10.3390/en15124201.

[54]   X. Huang *et al.*, "Shape-stabilized phase change materials based on porous supports for thermal energy storage applications," *Chemical Engineering Journal*, vol. 356, pp. 641–661, Jan. 2019, doi: 10.1016/j.cej.2018.09.013.

[55]   T. Wang, Y. Liu, R. Meng, and M. Zhang, "Thermal performance of galactitol/mannitol eutectic mixture/expanded graphite composite as phase change material for thermal energy harvesting," *J Energy Storage*, vol. 34, p. 101997, Feb. 2021, doi: 10.1016/j.est.2020.101997.

[56] G. T. Nguyen, T. N. Ly, N. T. Tran, H. N. A. Tuan, N. H. Hieu, and T. H. Bui, "Glutaric acid/expanded graphite composites as highly efficient shape-stabilized phase change materials at medium-temperature," *J Energy Storage*, vol. 63, p. 107038, Jul. 2023, doi: 10.1016/j.est.2023.107038.

[57] C. N. Thomas *et al.*, "Modeling the intensity and polarization response of planar bolometric detectors," *JOSAA*, vol. 27, no. 5, p. 1219, May 2010, doi: 10.1364/JOSAA.27.001219.

[58] Z. Liu *et al.*, "Mass production of biodegradable porous foam for simultaneous solar evaporation and thermoelectricity generation," *J Mater Chem A Mater*, vol. 11, no. 48, pp. 26784–26793, 2023, doi: 10.1039/D3TA06133G.

[59] Q. Wang, D. Zhou, Y. Chen, P. Eames, and Z. Wu, "Characterization and effects of thermal cycling on the properties of paraffin/expanded graphite composites," *Renew Energy*, vol. 147, pp. 1131–1138, Mar. 2020, doi: 10.1016/j.renene.2019.09.091.

[60] R. Radhakrishnan, K. E. Gubbins, A. Watanabe, and K. Kaneko, "Freezing of simple fluids in microporous activated carbon fibers: Comparison of simulation and experiment," *J Chem Phys*, vol. 111, no. 19, pp. 9058–9067, Nov. 1999, doi: 10.1063/1.480261.

[61] B. Tan *et al.*, "Preparation and thermal properties of shape-stabilized composite phase change materials based on polyethylene glycol and porous carbon prepared from potato," *RSC Adv*, vol. 6, no. 19, pp. 15821–15830, Feb. 2016, doi: 10.1039/C5RA25685B.

[62] C.-F. Wang *et al.*, "Synthesis and thermal conductivity of expanded graphite (EG)/polymer composites," in *2018 International Conference on Electronics Packaging and iMAPS All Asia Conference (ICEP-IAAC)*, IEEE, Apr. 2018, pp. 572–573. doi: 10.23919/ICEP.2018.8374653.

[63] S. Deng, J. Wang, G. Zong, F. Chen, S. Chai, and Q. Fu, "Effect of chain structure on the thermal conductivity of expanded graphite/polymer composites," *RSC Adv*, vol. 6, no. 12, pp. 10185–10191, 2016, doi: 10.1039/C5RA26272K.

[64] K. B., A. K. Pandey, R. Saidur, and V. V. Tyagi, "Energizing organic phase change materials using silver nanoparticles for thermal energy storage," *J Energy Storage*, vol. 58, p. 106361, Feb. 2023, doi: 10.1016/j.est.2022.106361.

[65] A. Anand, A. Shukla, A. Kumar, D. Buddhi, and A. Sharma, "Cycle test stability and corrosion evaluation of phase change materials used in thermal energy storage systems," *J Energy Storage*, vol. 39, Jul. 2021, doi: 10.1016/J.EST.2021.102664.

[66] C. Liang, K. Ruan, Y. Zhang, and J. Gu, "Multifunctional Flexible Electromagnetic Interference Shielding Silver Nanowires/Cellulose Films with Excellent Thermal Management and Joule Heating Performances," *ACS Appl Mater Interfaces*, vol. 12, no. 15, pp. 18023–18031, Apr. 2020, doi: 10.1021/acsami.0c04482.

[67] S. Pei, J. Teng, N. Ren, and S. You, "Low-Temperature Removal of Refractory Organic Pollutants by Electrochemical Oxidation: Role of Interfacial Joule Heating Effect," *Environ Sci Technol*, vol. 54, no. 7, pp. 4573–4582, Apr. 2020, doi: 10.1021/acs.est.9b05929.